J. Fluid Mech. (1980), *vol.* 97, *part* 3, *pp.* 481–512
Printed in Great Britain

Effects of the non-equilibrium condensation of vapour on the pressure wave produced by the collapse of a bubble in a liquid

By SHIGEO FUJIKAWA AND TERUAKI AKAMATSU
Department of Mechanical Engineering, Kyoto University, Kyoto

(Received 22 December 1978 and in revised form 2 July 1979)

Analytical and numerical analyses have been made of the physical behaviour of a collapsing bubble in a liquid. The mathematical formulation takes into account the effects of compressibility of the liquid, non-equilibrium condensation of the vapour, heat conduction and the temperature discontinuity at the phase interface. Numerical solutions for the collapse of the bubble are obtained beyond the time when the bubble reaches its minimum radius up to the stage when a pressure wave forms and propagates outward into the liquid. The numerical results indicate that evaporation and condensation strongly influence the dynamical behaviour of the bubble.

In addition, the propagation of the stress wave, both in a solid and a liquid, due to the collapse of the bubble has been observed by means of the dynamic photoelasticity. It is clearly demonstrated that the stress wave in a photoelastic specimen is caused by impact of the pressure wave radiated from the bubble.

1. Introduction

The main interest in cavitation bubble dynamics arises from the destructive action due to the collapse of bubbles in liquids near solid boundaries. Most of the theoretical and experimental efforts have been attempted in order to understand the mechanism by which the violent action of collapsing bubbles is brought to bear on the boundary.

Until now two different mechanisms have been theorized as the source of cavitation damage. One is that shock waves are radiated into the liquid when the collapsing motion of spherical bubbles is arrested (Hickling & Plesset 1964; Tomita & Shima 1977); in this case, the bubbles are supposed to contain only a small amount of non-condensable gas. The other mechanism is the impingement of liquid jets formed on bubbles in the neighbourhood of solid surfaces. This idea was first put forward by Kornfeld & Suvorov (1944). Then Naudé & Ellis (1961) and Plesset & Chapman (1971) showed that liquid jets may form on empty bubbles collapsing in the neighbourhood of solid boundaries. Recently Shima & Nakajima (1977) studied the problem of the collapse of a gaseous bubble attached to the solid boundary. They concluded that the cushioning effect of the internal gas weakened the jet or caused the bubble to rebound without the liquid jet.

The cushioning effect may be expected even for a purely vaporous bubble. Evaporation and condensation take place at a finite rate. If this rate is not high enough to keep up with the reducing rate of volume of the cavity, the vapour in the cavity will behave like a non-condensable gas. This so-called non-equilibrium effect on condensation will

0022–1120/80/4410–8560 $02.00

play an important role in the final collapsing stages when the inward radial velocity of the bubble wall increases rapidly (Plesset 1949; Zwick & Plesset 1955; Theofanus *et al.* 1969; Mitchell & Hammitt 1974). One of the objects of the present study is to elucidate the behaviours of the bubble collapse and the resulting pressure waves. In §§ 2, 3 and 4, the theoretical and numerical analyses will be made taking account of the effects of evaporation and condensation and temperature discontinuity at the interface, heat conduction inside the bubble and in the surrounding liquid, and compressibility of the liquid.

On the other hand, experiments on the collapse of bubbles have been performed by numerous investigators (Jones & Edwards 1960; Naudé & Ellis 1961; Kuttruff 1962; Benjamin & Ellis 1966; Kling & Hammitt 1972; Lauterborn & Bolle 1975). Jones & Edwards observed shock waves radiated into the liquid at the instant of the collapse of spark-induced bubbles. Kuttruff observed not only shock waves, but also flashes of sonoluminescent light from the ultrasonic cavitation. The others showed that the jets formed on bubbles collapsing near solid boundaries. Ebeling & Lauterborn (1977) observed, by cinematic holography, shock waves emanating from collapsing bubbles generated by laser pulses. Recently, by using a water shock tube, Fujikawa & Akamatsu (1975, 1978) found that an impulsive pressure accompanying the bubble collapse was caused by the impact of shock waves, and the jet impingement did not produce any detectable effects. However, the pressure gauge used in their experiments was not appropriate to measure the impact of microjet on the boundary, because the sensing area of the gauge (4 mm in diameter) was much larger than the impinging area of jet. In § 5, the above-mentioned observations will be re-examined using dynamic photoelasticity. Bubbles highly controlled both in location and time were made in the water-filled shock tube and photographs were taken of collapsing bubbles near the surface of a high-modulus photoelastic material. In fact, Ellis (1956) and Naudé & Ellis (1961) studied spark-induced bubbles using the photoelastic technique. However, because their photoelastic material was of low-modulus, they could not distinguish the stress waves due to the shock waves from those due to the jets and the background noise.

2. Formulation of bubble dynamics

2.1. *Statement of the problem and basic equations*

There is a spherical bubble of initial radius R_0 containing both vapour and non-condensable gas in a viscous compressible liquid. At time zero, the ambient pressure is increased instantaneously to $p_{l\infty}$, and then the bubble begins to collapse accompanied with phase change and heat conduction through the bubble wall. The problem is to investigate these physical effects on the bubble collapse and the pressure waves emanated from the bubble.

Schematic diagrams depicting a model and the temperature profile both inside and outside the bubble are illustrated in figure 1 (*a*, *b*). The temperature discontinuity in the non-equilibrium region existing at the interface is also shown in figure 1 (*b*).

In writing the basic equations, the following assumptions are made. (1) The bubble is spherically symmetric. (2) The effect of the interaction between compressibility and viscosity is negligible. (3) The effects of gravity and diffusion are negligible. (4) The pressure inside the bubble is uniform throughout. (5) The vapour and non-condensable

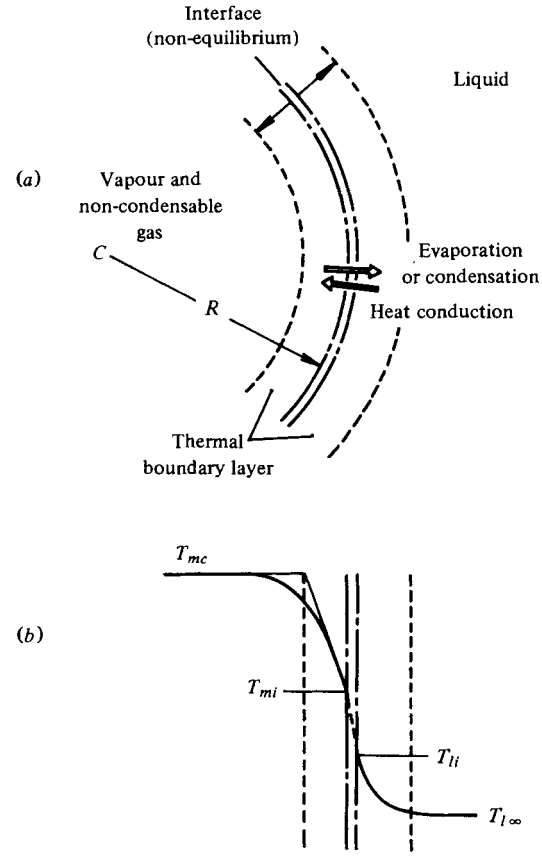

FIGURE 1. Schematic diagrams depicting the model (*a*) and the temperature profile both inside and outside the bubble (*b*).

gas are inviscid and obey the perfect-gas law. (6) The temperatures of the vapour and non-condensable gas are equal. (7) The thermal boundary layers developing both inside and outside the bubble are thin enough compared with the bubble radius. (8) There is a thin but finite non-equilibrium region at the phase interface because of the continuing process of phase change there. (9) The physical properties of liquid and gases are constant.

We introduce the assumptions (1)–(3) to facilitate the analysis since we wish to study mainly the effect of evaporation and condensation of the vapour on the collapse of the bubble and on the resulting pressure waves. The assumption (1) of spherical symmetry is, strictly speaking, invalid when a solid wall induces severe distortion in the bubble shape. However, several investigators (Kuttruff 1962; Fujikawa & Akamatsu 1975; Efimov *et al.* 1976) observed the shock wave radiation even from vaporous bubbles very close to the solid wall. The analysis based on this assumption will be the first step to elucidate the intensities of shock waves from real cavitation bubbles, in which heat conduction, non-equilibrium evaporation and condensation occur. The assumption (4) will remain valid so long as the velocity of the bubble wall is below the speed of sound in the vapour–gas mixture (Trilling 1952). With the assumption of a uniform pressure the momentum equation is of no consequence. The assumption

(5) will of course cease to be valid in the neighbourhood of the critical point. However it would seem to be difficult to use the Van der Waals equation as the equation of state, because the analysis becomes formidable. Therefore the molecular interaction is neglected in this paper as in Plesset & Prosperetti's (1976) paper. The assumption (6) will be approximately valid in the case where the molecular weights of the vapour and non-condensable gas are not extremely different as in the case of water vapour and air. The assumption (7), for the liquid layer surrounding the bubble wall, where evaporation and condensation take place, cannot in general be justified merely by the smallness of the Fourier number. With a view to this, the validity and the limitation of the thermal boundary-layer approximation are discussed in the appendix. The exact calculations of Hickling (1963) seem to suggest that it is possible to use the thin boundary-layer approximation for the gas side as well for the bubble contents although they were not intended for the total collapse of the bubble.

The assumption (8) of the non-equilibrium region is commonly made when studying the phase change. We can discuss the absolute rate of evaporation and condensation under this supposition. Finally, the assumption (9) ceases to be valid at the end of the collapse phase when the pressure and temperature of the bubble contents increase rapidly. However, it would seem to be extremely difficult to solve the free boundary-value problem whilst taking account of the time-dependent physical properties. The analysis based on the present assumptions will be the first step in an attempt to understand the behaviour of the collapse of true cavitation bubble in the liquid.

Under the above assumptions, the governing equations for the liquid and gases, and the boundary conditions at the interface may be expressed as follows.

In the external region occupied by the liquid

Continuity:
$$\frac{\partial \rho_l}{\partial t}+\frac{\partial}{\partial r}(\rho_l u_l)+\frac{2\rho_l u_l}{r}=0. \tag{1}$$

Momentum:
$$\frac{\partial u_l}{\partial t}+u_l\frac{\partial u_l}{\partial r}=-\frac{1}{\rho_l}\frac{\partial p_l}{\partial r}. \tag{2}$$

Energy:
$$\frac{\partial T_l}{\partial t}+u_l\frac{\partial T_l}{\partial r}=D\left(\frac{\partial^2 T_l}{\partial r^2}+\frac{2}{r}\frac{\partial T_l}{\partial r}\right). \tag{3}$$

Equation of state:
$$\frac{p_l+B}{p_{l\infty}+B}=\left(\frac{\rho_l}{\rho_{l\infty}}\right)^n. \tag{4}$$

In the above t is time, r the radial distance from the centre of the bubble, the suffix l represents the liquid, ρ_l is the density, $\rho_{l\infty}$ the density at infinity, u_l the radial particle velocity, p_l the pressure, $p_{l\infty}$ the pressure at infinity, T_l the temperature and D the thermal diffusivity of the liquid. In equation (4), B is 3010 atm and the index n is 7·15 for water. The validity of these values has been discussed elsewhere (Cole 1948).

In the internal region occupied by the mixture of the vapour and non-condensable gas

Continuity:
$$\frac{d}{dt}\int_V \rho_v\,dV=\int_S \dot{m}\,dS \quad \text{for the vapour;} \tag{5}$$

$$\frac{d}{dt}\int_V \rho_g\,dV=0 \quad \text{for the non-condensable gas.} \tag{6}$$

Here ρ_v and ρ_g are the densities of the vapour and non-condensable gas respectively, V and S the volume and surface area of the bubble. The expression for the rate of evaporation and condensation $\dot{m}$ of the vapour has the form (Schrage 1953)

$$\dot{m} = \frac{\alpha_M}{(2\pi R_v)^{\frac{1}{2}}}\left(\frac{p_v^*}{(T_{li})^{\frac{1}{2}}} - \Gamma.\frac{p_v}{(T_{mi})^{\frac{1}{2}}}\right), \tag{7}$$

in which α_M is the accommodation coefficient for evaporation or condensation (assumed constant), equal to the ratio of vapour molecules sticking to the phase interface to those impinging on it, p_v the actual vapour pressure, p_v^* the equilibrium vapour pressure, T_{mi} and T_{li} are the temperatures of the vapour and the liquid at the phase interface respectively, and R_v is the gas constant of the vapour. The correction factor Γ is expressed as follows,

$$\Gamma = \exp(-\Omega^2) - \Omega\sqrt{\pi}\left(1 - \frac{2}{\sqrt{\pi}}\int^{\Omega}\exp(-x^2)\,dx\right),$$

in which

$$\Omega = \frac{\dot{m}}{p_v}\left(\frac{R_v T_{mi}}{2}\right)^{\frac{1}{2}}.$$

Energy:

$$\rho_m\left(\frac{\partial e}{\partial t} + u_m\frac{\partial e}{\partial r}\right) = -\frac{p_m}{J}\left(\frac{\partial u_m}{\partial r} + \frac{2u_m}{r}\right) - \left(\frac{\partial q}{\partial r} + \frac{2q}{r}\right) \tag{8}$$

for the thermal boundary layer near the phase interface;

$$\frac{dE}{dt} + \frac{p_m}{J}\frac{dV}{dt} + \int_V \nabla.q\,dV - h\int_S \dot{m}\,dS = 0. \tag{9}$$

for the global contents within the bubble. The suffix m represents the mixture, p_m and ρ_m are the pressure and density of the vapour–gas mixture, u_m is the radial particle velocity, e the specific internal energy, E the internal energy of the global contents of the bubble, h the specific enthalpy of the vapour and J the mechanical equivalent of heat. The heat flux q is expressed as follows,

$$q = -\lambda_m\frac{\partial T_m}{\partial r},$$

in which T_m and λ_m are the temperature and thermal conductivity of the mixture, respectively. Equation (9) is the first law of thermodynamics for bulk flow through an open system (Hatsopoulos & Keenan 1965). The global contents of the bubble is taken here as the open thermodynamic system.

Equation of state:

$$p_v = \rho_v R_v T_m \quad \text{for the vapour;} \tag{10}$$

$$p_g = \rho_g R_g T_m \quad \text{for the noncondensable gas;} \tag{11}$$

$$p_m = \rho_m R_m T_m \quad \text{for the vapour–gas mixture.} \tag{12}$$

Here p_g is the pressure of the non-condensable gas, R_g and R_m are the gas constants of the non-condensable gas and the mixture respectively.

At the phase interface

Continuity:

$$[\rho_l(u_l-\dot{R})]_R = -\dot{m} \quad \text{for the liquid;} \tag{13}$$

$$[\rho_m(u_m-\dot{R})]_R = -\dot{m} \quad \text{for the vapour–gas mixture.} \tag{14}$$

R is the radius of the bubble, $\dot{R}$ the bubble wall velocity.

Momentum:

$$p_{l,R}+\frac{2\sigma}{R} = p_v+p_g+[\rho_m(u_m-\dot{R})(u_m-u_l)]_R+\frac{4\mu_l}{3}\left(\frac{\partial u_l}{\partial r}-\frac{u_l}{r}\right)_R, \tag{15}$$

where $p_{l,R}$ is the pressure in the liquid at the bubble wall, σ and μ_l are the surface tension and shear viscosity of the liquid respectively (Hsieh 1965).

Energy:

$$\lambda_l\left(\frac{\partial T_l}{\partial r}\right)_R = \lambda_m\left(\frac{\partial T_m}{\partial r}\right)_R+\dot{m}L, \tag{16}$$

where λ_l is the thermal conductivity of the liquid, and L the latent heat of evaporation or condensation.

Equilibrium vapour pressure (Clausius–Clapeyron equation):

$$p_v^* = p_c\exp\left(\frac{JL}{R_vT_c}\left(1-\frac{T_c}{T_{li}}\right)\right), \tag{17}$$

where p_c and T_c are the pressure and temperature at the critical state, for water 218·40 atm and 647·31 K, respectively.

Finally, one additional equation is needed, the temperature discontinuity at the gas–liquid interface (Kennard 1938; Schrage 1953). According to Kogan (1969), this discontinuity for the flow of gas inside the Knudsen layer in the neighbourhood of the boundary wall is expressed by the following:

$$T_{mi}-T_{li} = -\frac{(2-0{\cdot}827\alpha_T)\kappa_m\mu_m}{4(\kappa_m-1)\alpha_T P\rho_m}\left(\frac{2\pi}{R_mT_{li}}\right)^{\frac{1}{2}}\left(\frac{\partial T_m}{\partial r}\right), \tag{18}$$

where α_T is the thermal accommodation coefficient, P the Prandtl number of the mixture, μ_m the shear viscosity, and κ_m is the ratio of specific heats.

2.2. *Methods of analysis*

2.2.1. *The equation of motion of the liquid surrounding a collapsing bubble.* We begin this section with a general discussion of the motion of the compressible liquid during the bubble collapse. The formulation takes account of the effect of the non-equilibrium evaporation and condensation. The authors adopt the PLK method to account for liquid compressibility because this procedure is capable of an indefinitely high degree of accuracy. Benjamin (1958) first applied this method to solve the problem of the collapsing bubble and later Jahsman (1968) and Tomita & Shima (1977) further developed it. As expected, the present solution includes solutions previously obtained by these investigators as special cases.

Let $\Phi(r,t)$ be the velocity potential for the liquid. Then the continuity equation (1) and the momentum equation (2) take the following forms:

$$\frac{\partial\rho_l}{\partial t}+\rho_l\left(\frac{\partial^2\Phi}{\partial r^2}+\frac{2}{r}\frac{\partial\Phi}{\partial r}\right)+\left(\frac{\partial\Phi}{\partial r}\right)\left(\frac{\partial\rho_l}{\partial r}\right) = 0 \tag{19}$$

and
$$\frac{\partial\Phi}{\partial t}+\frac{1}{2}\left(\frac{\partial\Phi}{\partial r}\right)^2+\int\frac{dp_l}{\rho_l}=\text{const.} \tag{20}$$

From the equation (4) and the boundary conditions of $\Phi=0$, $p_l=p_{l\infty}$ at $r\to\infty$, the right-hand side of the equation (20) becomes const. $=c_\infty^2/(n-1)$. The sound speed c_∞ in the liquid at infinity is defined as follows:

$$c_\infty\equiv\left(\left(\frac{dp_l}{d\rho_l}\right)_\infty\right)^{\frac{1}{2}}=\left(\frac{n(p_{l\infty}+B)}{\rho_{l\infty}}\right)^{\frac{1}{2}}, \tag{21}$$

where $\rho_{l\infty}$ is the liquid density at infinity. Thus, from the equations (4) and (20), we obtain the sound speed in the liquid:

$$c^2=c_\infty^2-(n-1)\left[\partial\Phi/\partial t+\tfrac{1}{2}(\partial\Phi/\partial r)^2\right]. \tag{22}$$

Therefore, from the equations (19), (20) and (22), we obtain a partial differential equation concerning the velocity potential Φ,

$$\frac{\partial^2\Phi}{\partial r^2}+\frac{2}{r}\frac{\partial\Phi}{\partial r}-\frac{1}{c_\infty^2}\frac{\partial^2\Phi}{\partial t^2}=\frac{1}{c_\infty^2}\left[2.\frac{\partial\Phi}{\partial r}\frac{\partial^2\Phi}{\partial r\,\partial t}+\frac{2(n-1)}{r}\frac{\partial\Phi}{\partial r}\frac{\partial\Phi}{\partial t}\right.$$
$$\left.+(n-1)\frac{\partial^2\Phi}{\partial r^2}\frac{\partial\Phi}{\partial t}+\frac{n+1}{2}\left(\frac{\partial\Phi}{\partial r}\right)^2\frac{\partial^2\Phi}{\partial r^2}+\frac{n-1}{r}\left(\frac{\partial\Phi}{\partial r}\right)^3\right]. \tag{23}$$

The boundary conditions are:

(i) continuity at the phase interface

$$(\partial\Phi/\partial r)_R=\dot{R}-\dot{m}/\rho_l; \tag{24}$$

(ii) in the liquid at the interface the pressure equation

$$\left[\frac{\partial\Phi}{\partial t}+\frac{1}{2}\left(\frac{\partial\Phi}{\partial r}\right)^2\right]_R=\frac{c_\infty^2}{n-1}\left[1-\left(\frac{p_{l,R}+B}{p_{l\infty}+B}\right)^{(n-1)/n}\right]; \tag{25}$$

(iii) at infinity

$$\Phi=0\quad\text{as}\quad r\to\infty; \tag{26}$$

The initial conditions are:

$$\left.\begin{aligned}R&=R_0\\ \dot{R}_{+0}&=\frac{2c_\infty}{n-1}\left[\left(\frac{p_{l,R}+B}{p_{l\infty}+B}\right)^{(n-1/2n)}-1\right]_{+0}\end{aligned}\right\}\quad\text{at}\quad t=0. \tag{27}$$

Now, consider the problem along the outgoing characteristic $\eta(r,t)=$ const. such that

$$dt=(u_l+c)^{-1}dr\quad\text{on}\quad\eta=\text{const.} \tag{28}$$

According to the PLK method, we see

$$\left.\begin{aligned}\Phi(r,\eta)&=\phi_0(r,\eta)+\frac{1}{c_\infty}\phi_1(r,\eta)+\frac{1}{c_\infty^2}\phi_2(r,\eta)+\ldots,\\ r&=r,\\ t&=\eta+\frac{1}{c_\infty}t_1(r,\eta)+\frac{1}{c_\infty^2}t_2(r,\eta)+\ldots,\end{aligned}\right\} \tag{29}$$

where η is the initial time on the outgoing characteristic and satisfies the condition $\eta=t$ on $r=R$.

(i) *First perturbation procedure.* The first-order approximation $\Phi_1 (= \phi_0 + \phi_1/c_\infty)$ is determined by

$$\frac{\partial^2 \Phi_1}{\partial r^2} + \frac{2}{r}\frac{\partial \Phi_1}{\partial r} - \frac{1}{c_\infty^2}\frac{\partial^2 \Phi_1}{\partial t^2} = 0, \tag{30}$$

with the boundary conditions (24), (25) and (26). The appropriate solution can be written as follows:

$$\Phi_1(r, \eta) = -\frac{f(\eta)}{r}. \tag{31}$$

On the other hand, from equation (28), we obtain

$$t = \eta + \frac{r - R(\eta)}{c_\infty}. \tag{32}$$

An unknown function $f(\eta)$ in equation (31) can be determined from the boundary condition (24) by using equation (32):

$$f(\eta) = R^2\left(\dot{R} - \frac{\dot{m}}{\rho_{l\infty}}\right) - \frac{R^2}{c_\infty}\left[2\dot{R}\left(\dot{R} - \frac{\dot{m}}{\rho_{l\infty}}\right) + R\left(\ddot{R} - \frac{\dot{m}}{\rho_{l\infty}}\right)\right]. \tag{33}$$

Therefore, the velocity potential can be written as follows,

$$\Phi_1(r, \eta) = -\frac{1}{r}\left[R^2\left(\dot{R} - \frac{\dot{m}}{\rho_{l\infty}}\right) - \frac{R^2}{c_\infty}\left\{2\dot{R}\left(\dot{R} - \frac{\dot{m}}{\rho_{l\infty}}\right) + R\left(\ddot{R} - \frac{\dot{m}}{\rho_{l\infty}}\right)\right\}\right]. \tag{34}$$

From equations (24), (25) and (34), we obtain the equation of motion of the bubble with the first-order correction of the liquid compressibility and the effect of non-equilibrium evaporation and condensation:

$$R\ddot{R}\left(1 - \frac{2\dot{R}}{c_\infty} + \frac{\dot{m}}{\rho_{l\infty} c_\infty}\right) + \tfrac{3}{2}\dot{R}^2\left(1 + \frac{4\dot{m}}{3\rho_{l\infty} c_\infty} - \frac{4\dot{R}}{3c_\infty}\right) - \frac{\dot{m}R}{\rho_{l\infty}}\left(1 - \frac{2\dot{R}}{c_\infty} + \frac{\dot{m}}{\rho_{l\infty} c_\infty}\right)$$
$$- \frac{\dot{m}}{\rho_{l\infty}}\left(\dot{R} + \frac{\dot{m}}{2\rho_{l\infty}}\right) + \frac{p_{l\infty} - p_{\mathrm{II},R}}{\rho_{l\infty}} - \frac{R\dot{p}_{\mathrm{II},R}}{\rho_{l\infty} c_\infty} = 0, \tag{35}$$

where
$$p_{\mathrm{II},R} = -\frac{2\sigma}{R} + p_v + p_g - \frac{\dot{m}^2(\rho_{vi} + \rho_{gi} - \rho_{l\infty})}{\rho_{l\infty}(\rho_{vi} + \rho_{gi})} - \frac{4\mu_l}{R}\left(\dot{R} - \frac{\dot{m}}{\rho_{l\infty}}\right).$$

Here ρ_{vi} and ρ_{gi} are the densities of the vapour and non-condensable gas at the interface, respectively. The equation (35) is identical with that obtained by Tomita & Shima (1977) in case of $\dot{m} = \rho_{vi}\dot{R}$ and $\rho_{vi} = \text{const.}$, and furthermore, with equations by Herring (1941) and Trilling (1952) in case of $\dot{m} = 0$. The familiar result of Rayleigh (1917) is also deduced from the equation (35) for the special case when $\dot{R}/c_\infty \to 0$ and $\dot{m} = 0$.

(ii) *Second perturbation procedure.* Now, the right-hand side of the equation (23) is obtained from the first-order solution Φ_1, then the second-order correction ϕ_2 is determined by

$$\frac{\partial^2 \phi_2}{\partial r^2} + \frac{2}{r}\frac{\partial \phi_2}{\partial r} = -\frac{2f^3}{r^7}. \tag{36}$$

Under the boundary condition $\phi_2 = 0$ at $r \to \infty$, we have

$$\phi_2 = \frac{F(\eta)}{r} - \frac{R^6(\dot{R} - \dot{m}/\rho_{l\infty})^3}{10r^5}. \tag{37}$$

On the other hand, from equation (28), we obtain

$$t = \eta + \frac{r - R(\eta)}{c_\infty} + \frac{f(\eta)}{c_\infty^2}\left[\frac{1}{r} - \frac{1}{R(\eta)}\right]. \tag{38}$$

An unknown function $F(\eta)$ can be determined from the boundary condition (24) by using equation (38),

$$F(\eta) = \tfrac{1}{2}R^2\left(\dot{R} - \frac{\dot{m}}{\rho_{l\infty}}\right)^3 - 2R^2\dot{R}\left(\dot{R} - \frac{\dot{m}}{\rho_{l\infty}}\right)^2 - 2R^2\left(\dot{R} - \frac{\dot{m}}{\rho_{l\infty}}\right)(\dot{R}^2 + R\ddot{R})$$
$$- R^3\left(\ddot{R} - \frac{\ddot{m}}{\rho_{l\infty}}\right)\left[\left(5\dot{R} - \frac{\dot{m}}{\rho_{l\infty}}\right) - R^4\left(\dddot{R} - \frac{\dddot{m}}{\rho_{l\infty}}\right)\right]. \tag{39}$$

Thus, we can obtain the solution of Φ for the second-order approximation as follows:

$$\Phi_2(r,\eta) = -\frac{1}{r}\left[R^2\left(\dot{R} - \frac{\dot{m}}{\rho_{l\infty}}\right) - \frac{R^2}{c_\infty}\left\{2\dot{R}\left(\dot{R} - \frac{\dot{m}}{\rho_{l\infty}}\right) + R\left(\ddot{R} - \frac{\ddot{m}}{\rho_{l\infty}}\right)\right\}\right.$$
$$+ \frac{1}{c_\infty^2}\left\{-\tfrac{1}{2}R^2\left(\dot{R} - \frac{\dot{m}}{\rho_{l\infty}}\right)^3 + 2R^2\dot{R}\left(\dot{R} - \frac{\dot{m}}{\rho_{l\infty}}\right)^2 + 2R^2\left(\dot{R} - \frac{\dot{m}}{\rho_{l\infty}}\right)(\dot{R}^2 + R\ddot{R})\right.$$
$$\left.\left. + R^3\left(\ddot{R} - \frac{\ddot{m}}{\rho_{l\infty}}\right)\left(5\dot{R} - \frac{\dot{m}}{\rho_{l\infty}}\right) + R^4\left(\dddot{R} - \frac{\dddot{m}}{\rho_{l\infty}}\right) + \frac{R^6(\dot{R} - \dot{m}/\rho_{l\infty})^3}{10r^4}\right\}\right]. \tag{40}$$

Finally, we obtain the equation of motion of the bubble with the second-order correction of the liquid compressibility and the effect of non-equilibrium evaporation or condensation:

$$R\left(\ddot{R} - \frac{\ddot{m}}{\rho_{l\infty}}\right)\left[1 - \frac{1}{c_\infty}\left(2\dot{R} - \frac{\dot{m}}{\rho_{l\infty}}\right) + \frac{1}{c_\infty^2}\left(\frac{23}{10}\dot{R}^2 - \frac{31}{10}\frac{\dot{m}\dot{R}}{\rho_{l\infty}} - \frac{1}{5}\frac{\dot{m}^2}{\rho_{l\infty}^2}\right)\right]$$
$$+ \frac{3}{2}\left(\dot{R} - \frac{\dot{m}}{\rho_{l\infty}}\right)\left[\left(\dot{R} + \frac{1}{3}\frac{\dot{m}}{\rho_{l\infty}}\right) - \frac{4}{3}\frac{\dot{R}^2}{c_\infty} + \frac{1}{c_\infty^2}\left(\frac{7}{5}\dot{R}^3 - \frac{49}{30}\frac{\dot{m}\dot{R}^2}{\rho_{l\infty}} - \frac{14}{15}\frac{\dot{m}^2\dot{R}}{\rho_{l\infty}^2} - \frac{1}{6}\frac{\dot{m}^3}{\rho_{l\infty}^3}\right)\right]$$
$$+ \frac{1}{\rho_{l\infty}}\left[(p_{l\infty} - p_{l2,R}) - \frac{R\dot{p}_{l1,R}}{c_\infty} + \frac{1}{c_\infty^2}\left\{\left(2\dot{R} - \frac{\dot{m}}{\rho_{l\infty}}\right)R\dot{p}_{l1,R}\right.\right.$$
$$\left.\left. + (p_{l\infty} - p_{l1,R})\left[\tfrac{1}{2}\dot{R}^2 - \frac{3}{2}\frac{\dot{m}\dot{R}}{\rho_{l\infty}} - \frac{\dot{m}^2}{\rho_{l\infty}^2} + \frac{3}{2}\frac{(p_{l\infty} - p_{l1,R})}{\rho_{l\infty}}\right]\right\}\right] = 0, \tag{41}$$

where $$p_{l2,R} = p_{l1,R} + \frac{4\mu_l}{3c_\infty^2}\left[\frac{3\dot{m}}{2\rho_{l\infty}R}\left(\dot{R} - \frac{\dot{m}}{\rho_{l\infty}}\right)^2 - \frac{\dot{p}_{l1,R}}{\rho_{l\infty}} + \frac{\dot{m}(p_{l\infty} - p_{l1,R})}{\rho_{l\infty}^2 R}\right].$$

Disturbances on the bubble wall propagate through the liquid at the sound speed c along the outgoing characteristic (38).

Equation (41) is exactly accurate to second-order terms of the liquid compressibility and is, in case of $\dot{m} = \rho_{vi}\dot{R}$ and $\rho_{vi} = \text{const.}$, identical with that obtained by Tomita & Shima (1977). Terms with respect to $\dot{m}$ in this equation may be significant in the final collapsing stage when non-equilibrium evaporation and condensation become responsible for the behaviour of vaporous bubbles as well as liquid compressibility.

The pressure throughout the liquid can then be found from equations (4), (20) and (40):

$$p_l(r,t) = -B\left[1 - \frac{(p_{l\infty} + B)}{B}\left\{1 - \frac{(n-1)}{c_\infty^2}\left[\frac{\partial\Phi_2}{\partial t} + \frac{1}{2}\left(\frac{\partial\Phi_2}{\partial r}\right)^2\right]\right\}^{n/(n-1)}\right]. \tag{42}$$

2.2.2. *The temperature of the bubble contents at the interface.* We shall now proceed to obtain an approximate solution of the equation for thermal boundary layer in the internal gas region bounded by the bubble wall (see figure 1). The simple case without phase change was fully treated by Flynn (1975*a*, *b*). We will apply his method to solve the thermal boundary-layer equation under the boundary conditions with phase change. We first introduce the modified Lagrangian co-ordinates (z, t) related to the Eulerian co-ordinates (r, t) by the following relations:

$$z(r,t) = \int_0^r \xi^2 \rho_m(\xi, t)\, d\xi \Big/ \int_0^R \xi^2 \rho_m(\xi, t)\, d\xi, \tag{43}$$

where the z co-ordinate is such that $z = 0$ at the centre of the bubble ($r = 0$) and $z = 1$ at the phase interface ($r = R$). The denominator in the above equation measures essentially the mass of the fluid contained within the sphere of radius R, and it is a time-dependent function when the processes of evaporation, condensation, and diffusion take place across the gas–liquid interface. The introduction of these modified Lagrangian co-ordinates (z, t) as the independent variables offers the obvious advantage of immobilizing the mass of bubble contents. In terms of z and t, equation (8) may be transformed to

$$\frac{\partial T_m}{\partial t} - \frac{9\lambda_m}{C_{vm}\Theta^2} \cdot \frac{\partial}{\partial z}\left(\rho_m r^4 \frac{\partial T_m}{\partial z}\right) + \frac{3p_m}{C_{vm} J\Theta} \cdot \frac{\partial}{\partial z}(r^2 u_m) = 0, \tag{44}$$

where C_{vm} is the specific heat at constant volume of the mixture; and Θ is the function defined as follows:

$$\Theta = 3\int_0^R \xi^2 \rho_m(\xi, t)\, d\xi. \tag{45}$$

Here, for convenience, we introduce a function $\phi(z, t)$ such that

$$\frac{\partial \phi}{\partial z} = T_m - T_{l\infty}. \tag{46}$$

Then, equation (44) may be written by integration

$$\frac{\partial \phi}{\partial t} - \frac{9\lambda_m \rho_m r^4}{C_{vm}\Theta^2} \frac{\partial^2 \phi}{\partial z^2} + \frac{3}{C_{vm} J\Theta}\left[p_m r^2 u_m - \int_0^z r^2 u_m \frac{\partial p_m}{\partial z} dz\right] = \pi(t), \tag{47}$$

in which $\pi(t)$ is an arbitrary function of time. From equation (46),

$$\phi = \int_0^z (T_m - T_{l\infty})\, dz + \Sigma(t), \tag{48}$$

where the function $\Sigma(t)$ may be chosen such that

$$\pi(t) = 0 \quad \text{and} \quad \phi(z, 0) = 0, \tag{49}$$

if it is assumed that the temperature at $t = 0$ is $T_{l\infty}$ everywhere. We now approximate the density ρ_m by Θ/R^3 and introduce a new time variable χ defined by

$$\chi = 9\int_0^t \frac{\lambda_m(\xi)\, R(\xi)}{C_{vm}(\xi)\, \Theta(\xi)} d\xi. \tag{50}$$

Under the assumption that the pressure inside the bubble is uniform throughout, equation (47) becomes

$$\frac{\partial\phi}{\partial\chi}-\frac{\partial^2\phi}{\partial z^2}+\frac{3p_m r^2 u'_m}{C_{vm}J\Theta}=\left(\frac{r^4}{R^4}-1\right).\frac{\partial^2\phi}{\partial z^2} \tag{51}$$

where u'_m is the velocity, within the bubble, with respect to χ. The right-hand side of the equation (51) may be neglected because the factor (r^4/R^4-1) is extremely small near the interface ($r=R$) and also $\partial^2\phi/\partial z^2$ is small inside the bubble ($r<R$). We now introduce the assumption that the velocity within the bubble is a linear function of the radial (Flynn 1975*a*, *b*):

$$u'_m=\left(\dot{R}'-\frac{\dot{m}'}{\rho_{mi}}\right).\frac{r}{R}=\left(\dot{R}'-\frac{\dot{m}'}{\rho_{mi}}\right)z^{\frac{1}{3}}, \tag{52}$$

in which $\dot{R}'$ and $\dot{m}'$ are the velocity of the bubble wall and the rate of evaporation or condensation with respect to χ respectively, and the suffix i represents the interface. The right-hand side of the equation (52) was obtained by the approximation that $z\cong(r/R)^3$. Thus, from the equation (51) we obtain

$$\frac{\partial\phi}{\partial\chi}-\frac{\partial^2\phi}{\partial z^2}+\frac{3p_m R^2}{C_{vm}J\Theta}\left(\dot{R}'-\frac{\dot{m}'}{\rho_{mi}}\right).z=0. \tag{53}$$

The form of this differential equation permits us to define a new dependent variable

$$W(z,\chi)=\phi(z,\chi)+z\psi(\chi), \tag{54}$$

where

$$\psi(\chi)=\frac{3}{J}\int_0^\chi\frac{p_m R^2}{C_{vm}\Theta}\left(\dot{R}'-\frac{\dot{m}}{\rho_{mi}}\right)d\xi. \tag{55}$$

Then, the equation (53) reduces to

$$\frac{\partial W}{\partial\chi}=\frac{\partial^2 W}{\partial z^2}, \tag{56}$$

with the initial and boundary conditions

$$W(z,0)=0, \tag{57}$$

$$W(0,\chi)=0, \tag{58}$$

$$\left(\frac{\partial W}{\partial z}\right)_{z=1}=\psi_1(\chi), \tag{59}$$

and in which

$$\psi_1(\chi)=\psi(\chi)+T_{mi}(\chi)-1. \tag{60}$$

The appropriate solution of the equation (56) is

$$W(z,\chi)=-\int_0^\chi\vartheta_1[\tfrac{1}{2}z\,|\,i\pi\xi]\,\psi_1(\psi\chi-\xi)\,d\xi, \tag{61}$$

where ϑ_1 is a theta function of the first kind defined by

$$\vartheta_1[\tfrac{1}{2}z\,|\,i\pi\chi]=i\sum_{n=-\infty}^{\infty}(-1)^n\exp[-\pi^2(n-\tfrac{1}{2})^2\chi+i\pi(n-\tfrac{1}{2})z]. \tag{62}$$

From the equation (61), we can obtain the gradient of temperature inside the bubble in the following form:

$$\frac{\partial T_m}{\partial z}=-\int_0^\chi\vartheta_1[\tfrac{1}{2}z\,|\,i\pi\xi]\,\frac{d\psi_1(\chi-\xi)}{d(\chi-\xi)}\,d\xi. \tag{63}$$

Here, define an auxiliary function $h_k(z, \chi)$ by

$$h_k(z, \chi) = \sin[\tfrac{1}{2}(2k+1)\pi z] H_k(\chi) \quad (k = 0, 1, 2, 3, \ldots), \tag{64}$$

in which

$$H_k(\chi) = \frac{C_{vm}}{3} \exp[-\tfrac{1}{4}(2k+1)^2\pi^2\chi] \int_0^\chi \exp[\tfrac{1}{4}(2k+1)^2\pi^2 x] \frac{d\psi_1}{dx} dx. \tag{65}$$

From the equations (50), (55), (60) and (65), we obtain

$$\frac{dH_k}{dt} + \frac{9(2k+1)^2\pi^2\lambda_m R}{4C_{vm}\Theta} H_k - \frac{p_m R^2}{J\Theta}\left(\dot{R} - \frac{\dot{m}}{\rho_{mi}}\right) - \frac{C_{vm}}{3}\frac{dT_{mi}}{dt} = 0. \tag{66}$$

Then, the equation (63) may be expressed by the following:

$$\left.\begin{aligned} \frac{\partial T_m}{\partial z} &= \frac{6}{C_{vm}} \sum_{k=0}^{\infty} (-1)^k h_k(z, t) \\ \text{or} \qquad &= \frac{6}{C_{vm}} \sum_{k=0}^{\infty} (-1)^k H_k(t) \sin[\tfrac{1}{2}(2k+1)\pi z]. \end{aligned}\right\} \tag{67}$$

In particular, the temperature gradient of the bubble contents at the phase interface ($z = 1$) becomes

$$\left(\frac{\partial T_m}{\partial r}\right)_R = \frac{18}{C_{vm} R} \sum_{k=0}^{\infty} H_k(t). \tag{68}$$

From the equations (18) and (68), we obtain the temperature of the bubble contents at the interface as follows:

$$T_{mi} = T_{li} - \frac{9(2 - 0{\cdot}827\alpha_T)\kappa_m \mu_m}{2(\kappa_m - 1)\alpha_T C_{vm} P \rho_m R}\left(\frac{2\pi}{R_m T_{li}}\right)^{\frac{1}{2}} \sum_{k=0}^{\infty} H_k(t). \tag{69}$$

2.2.3. *The temperature at the centre and the pressure of the bubble contents.* For simplicity, we assume the temperature distribution within the bubble to be

$$\left.\begin{aligned} T_m &= T_{mc} \quad \text{when} \quad 0 \leqslant r \leqslant R - \delta \\ \text{and} \qquad T_m &= T_{mi} - \left(\frac{\partial T_m}{\partial r}\right)_R . (r - R) \quad \text{when} \quad R - \delta \leqslant r \leqslant R, \end{aligned}\right\} \tag{70}$$

where T_{mc} is the temperature at the bubble centre; and δ is the thermal boundary-layer thickness defined by

$$\delta = \frac{(T_{mc} - T_{mi})}{(\partial T_m/\partial r)_R}. \tag{71}$$

As the bubble collapse proceeds, the temperature of the bubble contents tends to become spatially uniform (Hickling 1963); the interfacial temperature approaches that at the centre and the thermal boundary-layer thickness δ becomes small in comparison with the bubble radius.

Substituting equation (70) into equations (5) and (6), and arranging them by using the equations of state, (10) and (11), we obtain

$$\frac{dp_v}{dt} - \theta_{v1}\frac{dT_{mc}}{dt} - \theta_{v2} = 0 \tag{72}$$

and

$$\frac{dp_g}{dt} - \theta_{g1}\frac{dT_{mc}}{dt} - \theta_{g2} = 0, \tag{73}$$

where

$$\theta_{v1} = \left[\frac{p_v\delta}{(T_{mc}-T_{mi})}\left\{\frac{(R-\delta)^2}{T_{mc}}+\frac{1}{(T_{mc}-T_{mi})}\left[I+\delta\left\{2\alpha\delta+2R-\delta+2(\alpha\delta+R)\,\alpha\ln\left(\frac{T_{mi}}{T_{mc}}\right)\right\}\right]\right\}\right.$$
$$+p_v\left\{\frac{(R-\delta)^3}{3T_{mc}^2}-\delta\left[\frac{(\alpha\delta+R)^2}{T_{mc}(T_{mc}-T_{mi})}+\frac{I}{(T_{mc}-T_{mi})^2}+\frac{T_{mi}\delta}{(T_{mc}-T_{mi})^3}\right.\right.$$
$$\left.\left.\times\left\{\delta+2(\alpha\delta+R)\ln\left(\frac{T_{mi}}{T_{mc}}\right)\right\}\right]\right\}\Bigg/\left[\frac{(R-\delta)^3}{3T_{mc}}-\frac{I.\delta}{(T_{mc}-T_{mi})}\right], \tag{74}$$

$$\theta_{v2} = \left[p_v\delta\left\{\frac{(\delta-\beta)}{\beta(T_{mc}-T_{mi})}\left[\frac{(R-\delta)^2}{T_{mc}}+\frac{I}{(T_{mc}-T_{mi})}+\frac{\delta}{(T_{mc}-T_{mi})}\right.\right.\right.$$
$$\left.\times\left\{2\alpha\delta+2R-\delta+2(\alpha\delta+R)\,\alpha\ln\left(\frac{T_{mi}}{T_{mc}}\right)\right\}\right]+\frac{1}{(T_{mc}-T_{mi})}$$
$$\left.\times\left[\frac{(\alpha\delta+R)^2}{T_{mi}}+\frac{I}{(T_{mc}-T_{mi})}+\frac{T_{mc}\delta}{(T_{mc}-T_{mi})^2}\left\{\delta+2(\alpha\delta+R)\ln\left(\frac{T_{mi}}{T_{mc}}\right)\right\}\right]\right\}\frac{dT_{mi}}{dt}$$
$$+\dot{m}R^2R_v-p_v\dot{R}\left\{\frac{(R-\delta)^2}{T_{mc}}-\frac{2\delta}{(T_{mc}-T_{mi})}\left[\delta+(\alpha\delta+R)\ln\left(\frac{T_{mi}}{T_{mc}}\right)\right]\right\}-\frac{p_v\delta^2}{\beta(T_{mc}-T_{mi})}$$
$$\left.\times\left\{\frac{(R-\delta)^2}{T_{mc}}+\frac{1}{(T_{mc}-T_{mi})}\left[I+\delta\left\{2\alpha\delta+2R-\delta+2(\alpha\delta+R)\,\alpha\ln\left(\frac{T_{mi}}{T_{mc}}\right)\right\}\right]\right\}\frac{dT_{li}}{dt}\right]\Bigg/$$
$$\div\left[\frac{(R-\delta)^3}{3T_{mc}}-\frac{I.\delta}{(T_{mc}-T_{mi})}\right]. \tag{75}$$

Here

$$\left.\begin{aligned}\alpha &= \frac{T_{mi}}{(T_{mc}-T_{mi})},\\ \beta &= -\frac{(2-0{\cdot}827\alpha_T)\,\kappa_m\mu_m}{4(\kappa_m-1)\,\alpha_T P\rho_m}\left(\frac{2\pi}{R_m T_{li}}\right)^{\frac{1}{2}},\\ I &= \int_{-1}^{0}\frac{(\delta.\xi+R)^2}{\xi-\alpha}\,d\xi.\end{aligned}\right\}$$

Replacing p_v and $\dot{m}$ by p_g and zero respectively, we can obtain θ_{g1} from the equation (74) and θ_{g2} from equation (75).

Thus, the equation concerning the temperature at the bubble centre may be obtained from the equations (9), (70), (72) and (73) in the following form:

$$\frac{dT_{mc}}{dt} = -\frac{3[p_v(\kappa_g-1)+p_g(\kappa_v-1)]\,\dot{R}}{[\theta_{v1}(\kappa_g-1)+\theta_{g1}(\kappa_v-1)]\,R}-\frac{[\theta_{v2}(\kappa_g-1)+\theta_{g2}(\kappa_v-1)]}{[\theta_{v1}(\kappa_g-1)+\theta_{g1}(\kappa_v-1)]}$$
$$-\frac{3J(\kappa_v-1)\,(\kappa_g-1)}{[\theta_{v1}(\kappa_g-1)+\theta_{g1}(\kappa_v-1)]\,R}\cdot\left[\frac{p_m}{J}\dot{R}-\frac{18\lambda_m}{C_{vm}R}\sum_{k=0}^{\infty}H_k(t)-C_{pv}T_{mi}\dot{m}\right], \tag{76}$$

in which κ_v and κ_g are the ratios of specific heats of the vapour and non-condensable gas respectively; C_{pv} is the specific heat at constant pressure of the vapour.

Initial conditions of the equations (72), (73) and (76) are:

$$p_v = p_v^*, \quad p_g = p_{g0}, \quad T_{mc} = T_{mi}. \tag{77), (78), (79}$$

2.2.4. *The temperature in the liquid at the interface.* In addition to the equation (16) we have the following initial and boundary conditions:

$$T_l(r, 0) = T_{l\infty}, \tag{80}$$

$$T_l(r, t) = T_{l\infty} \quad \text{as} \quad r \to \infty, \tag{81}$$

in which $T_{l\infty}$ is the liquid temperature at infinity. An approximate solution to the problem posed by the equations (3), (16), (80), and (81) was obtained by Plesset & Zwick (1952) under the assumption that appreciable temperature gradients are established only in a thin layer surrounding the bubble wall. The zeroth-order solution and the first-order correction for the bubble surface temperature T_{li} may be summarized as follows:

$$T_{li} = T_{l\infty} - \left(\frac{D}{\pi}\right)^{\frac{1}{2}} \left[\int_0^{\epsilon} \frac{G(\zeta)\, d\zeta}{(\epsilon - \zeta)^{\frac{1}{2}}} - 2 \int_0^{\epsilon} \frac{d\xi}{R^3(\xi)} \int_0^{\xi} \frac{\theta^0(\zeta)}{(\epsilon - \zeta)^3} \left(1 - 3\frac{\epsilon - \xi}{\epsilon - \zeta} \right) d\zeta \right], \tag{82}$$

in which

$$\left.\begin{aligned} \epsilon(t) &= \int_0^t R^4(\xi)\, d\xi, \\ G(t) &= \frac{\dot{m} L}{\lambda_l R^2} + \frac{18 \lambda_m}{\lambda_l C_{vm} R^3} \sum_{k=0}^{\infty} H_k(t), \\ \theta^0(\zeta) &= -\left(\frac{D}{\pi}\right)^{\frac{1}{2}} \int_0^{\zeta} \frac{G(\zeta)\, d\zeta}{(\epsilon - \zeta)^{\frac{1}{2}}}. \end{aligned}\right\}$$

3. Numerical results and discussions

All physical quantities involving length, time, velocity and so on, may now be made dimensionless through the following normalization, primes indicating the dimensionless quantities:

$$r' = \frac{r}{R_0}, \quad R' = \frac{R}{R_0}, \quad t' = \frac{t}{R_0}\left(\frac{p_{l\infty}}{\rho_{l\infty}}\right)^{\frac{1}{2}}, \quad \dot{R}' = \dot{R}\left(\frac{\rho_{l\infty}}{p_{l\infty}}\right)^{\frac{1}{2}}, \quad \ddot{R}' = \ddot{R}\frac{\rho_{l\infty} R_0}{p_{l\infty}},$$

$$p' = \frac{p}{p_{l\infty}}, \quad T' = \frac{T}{T_{l\infty}}, \quad \rho' = \frac{\rho}{\rho_{l\infty}}, \quad \dot{m}' = \frac{\dot{m}}{(\rho_{l\infty} p_{l\infty})^{\frac{1}{2}}}, \quad \dot{m}' = \dot{m}\frac{R_0}{p_{l\infty}},$$

$$\mu' = \frac{\mu}{R_0(\rho_{l\infty} p_{l\infty})^{\frac{1}{2}}}, \quad \sigma' = \frac{\sigma}{R_0 p_{l\infty}}, \quad c'_{\infty} = c_{\infty}\left(\frac{\rho_{l\infty}}{p_{l\infty}}\right)^{\frac{1}{2}}, \quad R' = R\frac{\rho_{l\infty} T_{l\infty}}{p_{l\infty}},$$

$$C'_v = \frac{C_v}{C_{lv}}, \quad C'_p = \frac{C_p}{C_{lv}}, \quad L' = \frac{L}{C_{lv} T_{l\infty}}, \quad D' = \frac{D}{R_0}\left(\frac{\rho_{l\infty}}{p_{l\infty}}\right)^{\frac{1}{2}}, \quad \lambda' = \frac{\lambda}{C_{lv} R_0 (\rho_{l\infty} p_{l\infty})^{\frac{1}{2}}},$$

$$J' = J\frac{\rho_{l\infty} C_{lv} T_{l\infty}}{p_{l\infty}}.$$

All the equations are rewritten in dimensionless form, but retain virtually the same forms as those without the primes.

Differential equations (41), (66), (72), (73), and (76) were numerically integrated by the Runge–Kutta–Gill method on the digital computer FACOM M-190 in the Computing Center, Kyoto University. For comparison with our experimental data obtained by the water shock tube, the following initial conditions were chosen: $R_0 = 1{\cdot}0\,\text{mm}$, $T_{l\infty} = 293{\cdot}15\,\text{K}$, $p_{l\infty} = 0{\cdot}7025$ atm, $p_{g0} = 0$ and $0{\cdot}01 p_{l\infty}$ atm,

Density (water)	ρ_l	998·2	kg m^{-3}
Shear viscosity (water)	μ_l	$1{\cdot}022 \times 10^{-4}$	kg s m^{-2}
Shear viscosity (air)	μ_g	$1{\cdot}86 \times 10^{-6}$	kg s m^{-2}
Shear viscosity (water vapour)	μ_v	$1{\cdot}28 \times 10^{-6}$	kg s m^{-2} (100 °C)
Surface tension (water-saturated vapour)	σ	$7{\cdot}20 \times 10^{-3}$	kg m^{-1}
Gas constant (air)	R_g	29·27	kg m kg^{-1} K^{-1}
Gas constant (water vapour)	R_v	47·06	kg m kg^{-1} K^{-1}
Thermal conductivity (water)	λ_l	$1{\cdot}43 \times 10^{-4}$	kcal m^{-1} s^{-1} °C^{-1}
Thermal conductivity (air)	λ_g	$6{\cdot}11 \times 10^{-6}$	kcal m^{-1} s^{-1} °C^{-1}
Thermal conductivity (water vapour)	λ_v	$5{\cdot}78 \times 10^{-6}$	kcal m^{-1} s^{-1} °C^{-1} (100 °C)
Thermal diffusivity (water)	D_l	$1{\cdot}43 \times 10^{-7}$	m^2 s^{-1}
Specific heat (water)	C_{lv}	0·998	kcal kg^{-1} °C^{-1}
Specific heat at constant pressure (air)	C_{pg}	0·240	kcal kg^{-1} °C^{-1}
Specific heat at constant pressure (water vapour)	C_{pv}	0·444	kcal kg^{-1} °C^{-1}
Specific heat at constant volume (air)	C_{vg}	0·171	kcal kg^{-1} °C^{-1}
Specific heat at constant volume (water vapour)	C_{vv}	0·334	kcal kg^{-1} °C^{-1}
Ratio of specific heats (air)	κ_g	1·40	
Ratio of specific heats (water vapour)	κ_v	1·33	
Latent heat	L	585·47	kcal kg^{-1}
Prandtl number (air)	P_g	0·71	
Prandtl number (water vapour)	P_v	1·12 (100 °C)	
Sound speed (water)	c_∞	1483	m s^{-1}
Mechanical equivalent of heat	J	426·8	kg m kcal^{-1}

TABLE 1. Physical properties (at 1 atm, 20 °C)

$p_{v0} = 0{\cdot}02305$ atm, $\alpha_M = 0$, 0·01, 0·04, 0·1 and 1·0. The water molecule is polar and, of course, rather asymmetrical, so that the accommodation coefficient for condensation α_M could very well be a small number (Knacke & Stranski 1956). Alty & Mackay (1935), Hill (1966) and Mori *et al.* (1973) made experiments for the water vapour and concluded that $\alpha_M \cong 0{\cdot}04$. Therefore the numerical results are shown mainly for the value $\alpha_M = 0{\cdot}04$. As to the thermal accommodation coefficient, the value obtained by Alty (1936) and Hill (1966), $\alpha_T = 1{\cdot}0$, was adopted in this study. The physical properties of water, water vapour, and air are shown in table 1.

Figures 2–8 are concerned with the behaviour of a bubble for $p_{g0} = 0{\cdot}01 p_{l\infty}$ and $\alpha_M = 0{\cdot}04$. The results are compared with the behaviour of the bubble containing air undergoing an adiabatic process and the saturated vapour, which is indicated by chained lines with one dot.

Figure 2 shows the time history of the bubble radius. In the case in which the evaporation and condensation of water vapour and the heat conduction take place at the bubble wall, the bubble contracts slowly in the final stages of the collapse in comparison with the adiabatic case. The damped ratio of the maximum radius $P_{\max}$ of the rebounding bubble, $(|R_0 - R_{\max}|/R_0 \times 100)$, is 19·4 % for thebubble with evaporation or condensation and heat conduction, and is 17·2 % for the adiabatic bubble. The damping of the bubble oscillation is caused by the effects of liquid compressibility, evaporation or condensation and heat conduction.

Figure 3 shows the time histories of the bubble wall velocity $V(\equiv \dot{R})$ and the

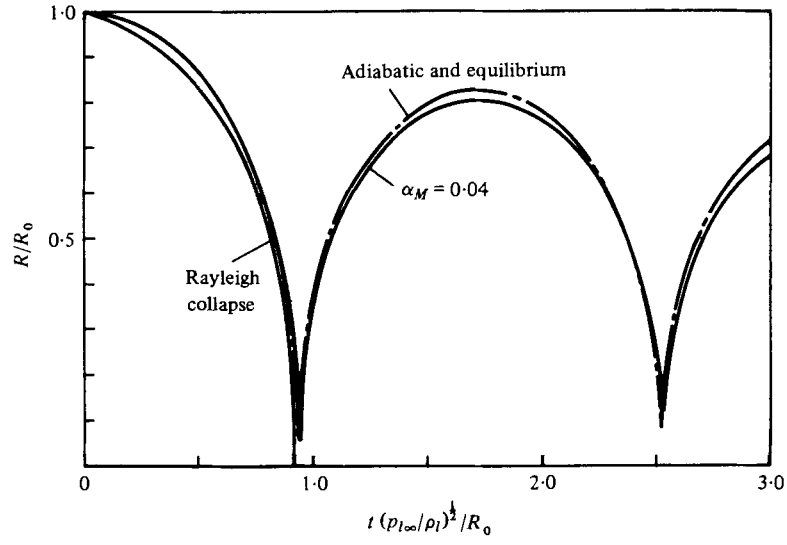

FIGURE 2. The time history of the bubble radius.

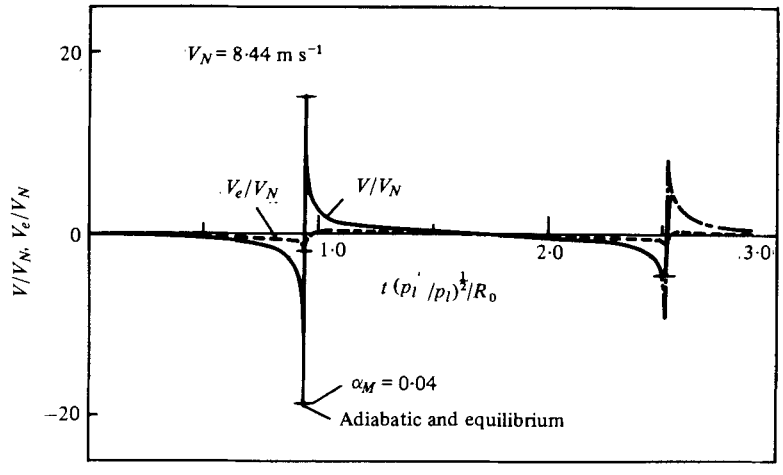

FIGURE 3. The time histories of the bubble-wall velocity and characteristic velocity of evaporation or condensation.

characteristic velocity of evaporation and condensation V_e. The latter V_e is defined by the following:

$$V_e = \alpha_M \left(\frac{R_v T_{li}}{2\pi}\right)^{\frac{1}{2}} \left[\frac{\rho_{vi}^*(T_{li})}{\rho_{vi}} - \Gamma\left(\frac{T_{mi}}{T_{li}}\right)^{\frac{1}{2}}\right],$$

where ρ_{vi}^* is the equilibrium vapour density at the phase interface. The actual vapour pressure within the bubble mainly depends on the relations between V and V_e. That is, if $V > V_e$, the vapour pressure will increase because of high rates of compression. If $V \leqslant V_e$, the vapour pressure will be kept in an equilibrium state. In the case of figure 3, $|V|$ is always greater than $|V_e|$, and the difference between $|V|$ and $|V_e|$ tends to increase as the bubble collapses. The wall velocity of the bubble collapsing with condensation and heat conduction is slightly low in comparison with the case of adiabatic collapse. The vapour still continues to condense during 4·3 μs immediately after the first rebound owing to the non-equilibrium effect of condensation.

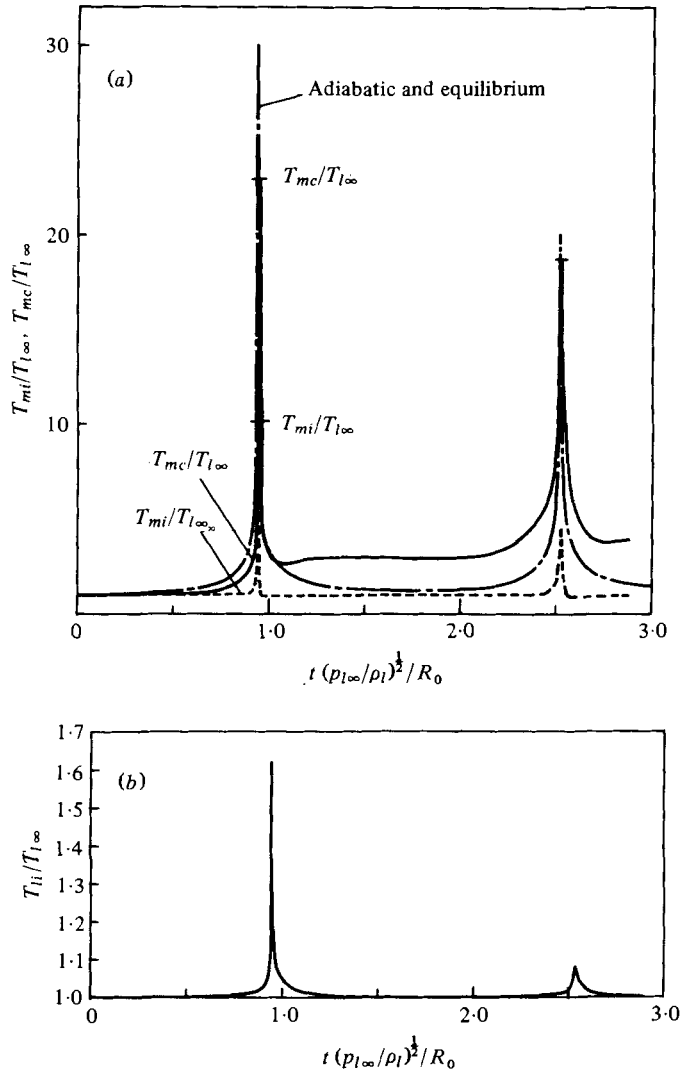

FIGURE 4. The time histories of the temperatures of the bubble contents (*a*) and liquid (*b*).

Figure 4 shows the time histories of the temperature of the bubble contents (*a*) and the liquid (*b*). In this case, the maximum temperatures at the centre and at the interface of bubble are 6700 K and 3413 K respectively. These temperatures are much lower than those in the adiabatic collapse (8786 K). The temperature throughout the bubble contents is not uniform because of heat conduction at the interface. The interfacial temperature of the bubble falls to 292·4 K at a time 2 μs after the first rebound, because the bubble rapidly expands. The temperature at the bubble centre, on the other hand, decreases adiabatically during 11·4 μs after the rebound, and then it is maintained at about 870 K. The maximum interfacial temperature of the liquid is 474 K. The temperature discontinuity at the interface increases as the bubble collapse proceeds.

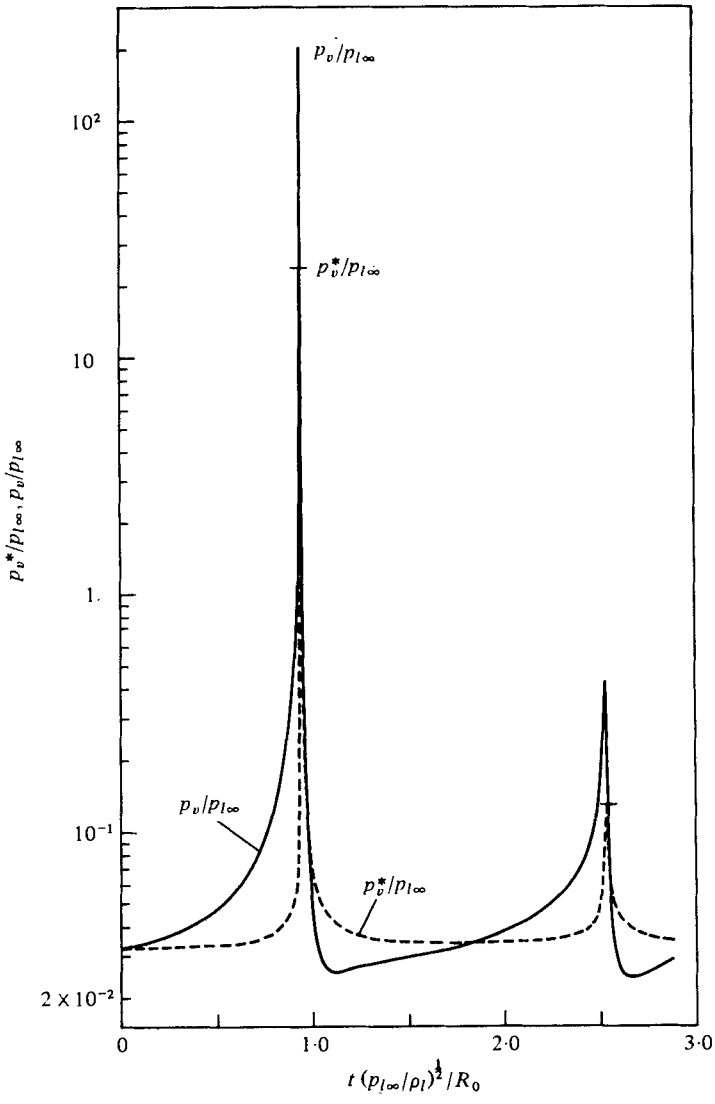

FIGURE 5. The time history of the vapour pressure within the bubble.

Figure 5 shows the time history of the vapour pressure within the bubble. In this case, the maximum vapour pressure $p_{v\max}$ is 144 atm, while the maximum equilibrium vapour pressure $p^*_{v\max} = 15{\cdot}6$ atm. The actual vapour pressure deviates from the equilibrium pressure in the final stages of collapse.

Figure 6 shows the time history of the gas (air) pressure within the bubble. The gas pressure almost adiabatically varies, and attains to 848 atm when the bubble contracts to its minimum radius. Meanwhile, in the case of adiabatic collapse, the maximum gas pressure is 1033 atm.

Figures 7 (*a*) and (*b*) show the pressure distributions in the liquid before and after the collapse of the bubble containing gas and water vapour. The comparison of the result

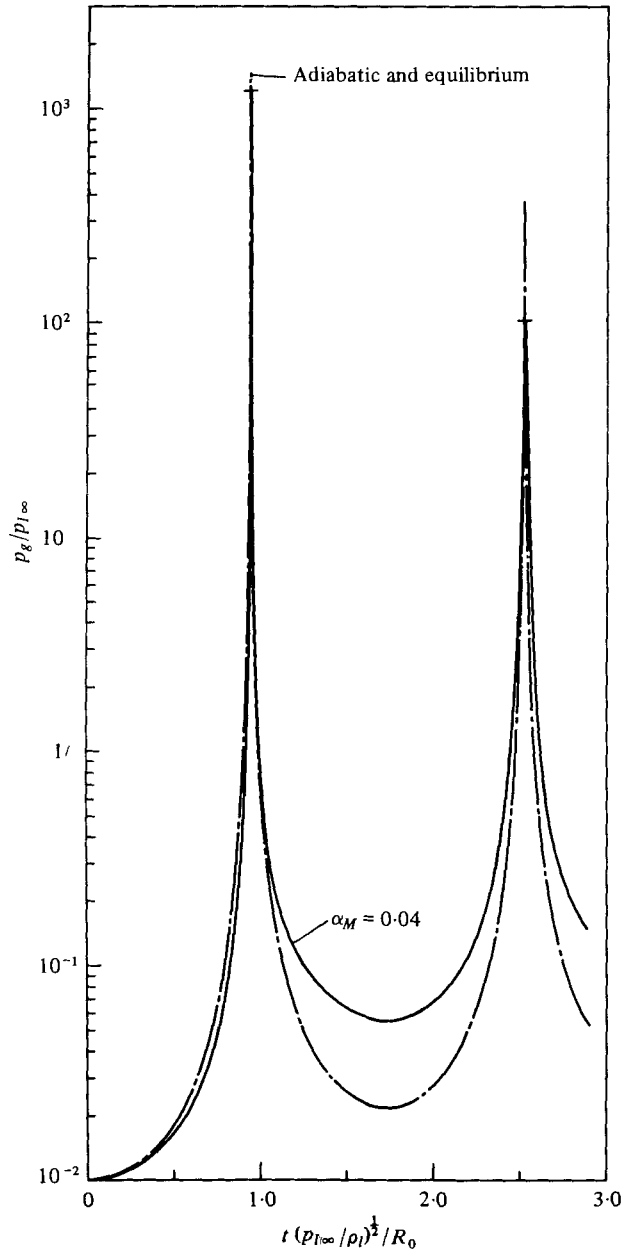

FIGURE 6. The time history of the gas pressure within the bubble.

of the present calculation with the adiabatic collapse (Tomita & Shima 1977) is made for nearly the same bubble radii. In these figures, dotted lines indicate the pressure at the bubble wall, and dashed lines represent the locus of the instantaneous peak pressure. The time is defined in dimensionless form as follows:

$$\tau = \frac{t}{R_0}\left(\frac{p_{l\infty}}{\rho_{l\infty}}\right)^{\frac{1}{2}},$$

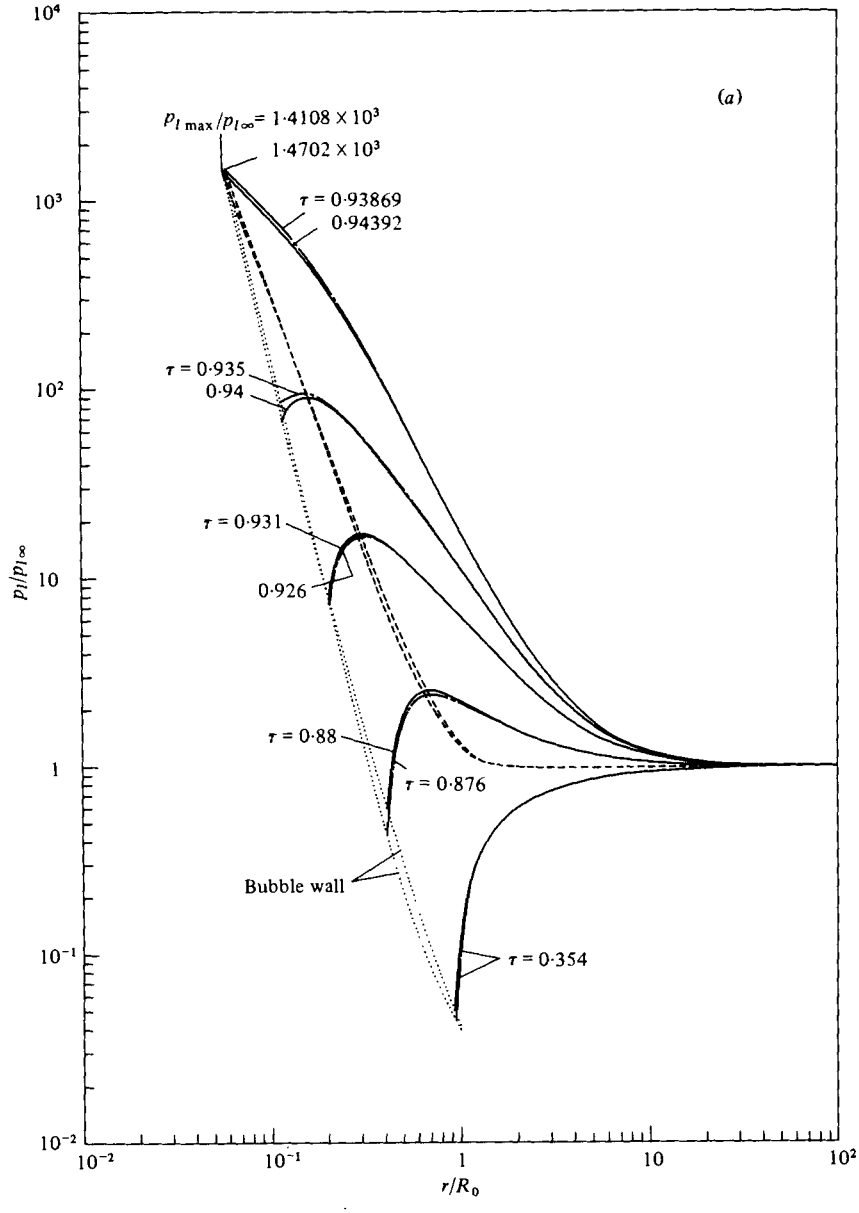

FIGURE 7 (*a*). For legend see facing page.

where t is the time elapsed from the start of the collapse. In the early stages of the collapse the pressure in liquid is slightly lower than that in the adiabatic case, but in the final stages becomes higher than it. The attained maximum impulsive pressures are 991 atm for the present calculation and 1033 atm for the adiabatic collapse. The pressure in liquid attenuates by the effect of liquid compressibility and, at the instant when the bubble attains its minimum radius, the pressure, at the position $r/R_0 = 1$, is 13 atm (the same value as in the adiabatic case). Figure 7 (*b*) shows that the pressure wave forms and travels outwards into the liquid after the rebound. The

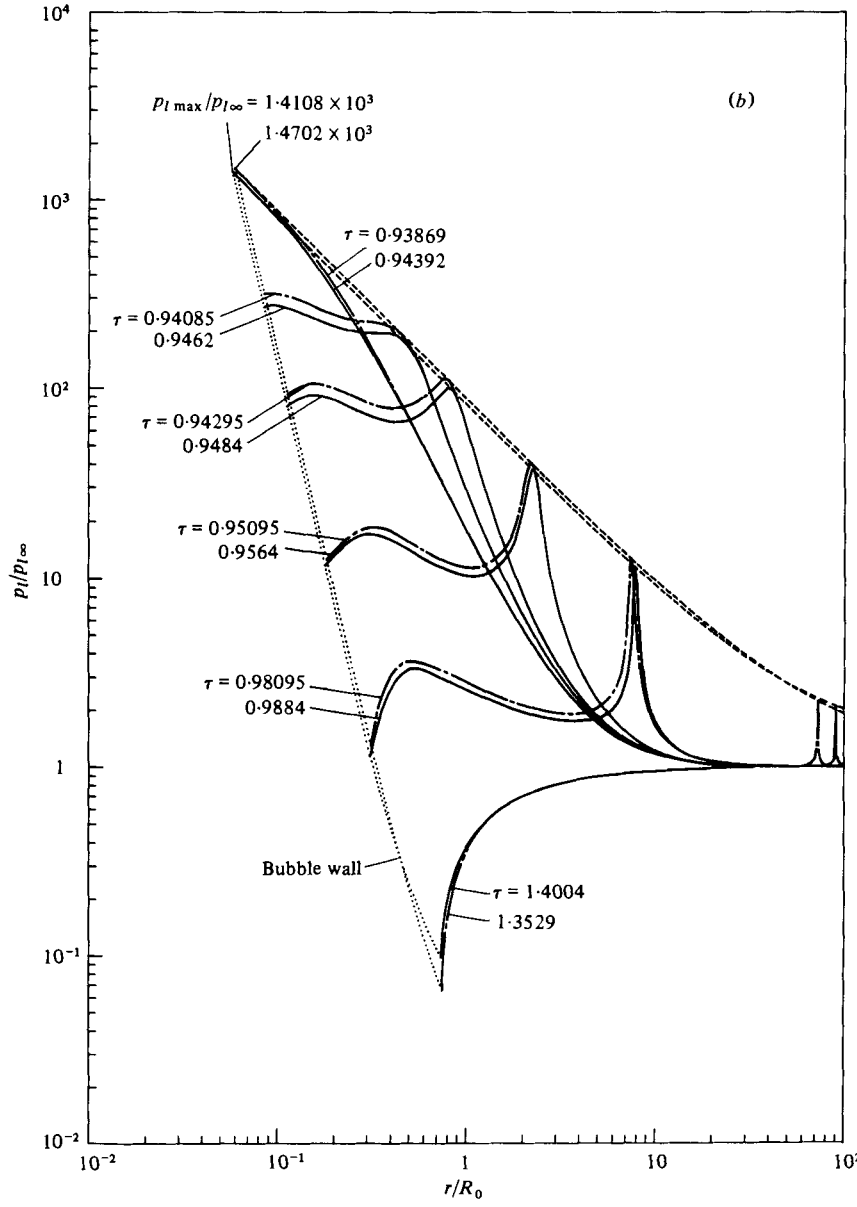

FIGURE 7. The pressure distributions in liquid (*a*) before and (*b*) after the collapse of a vapour–gas bubble with initial radius R_0 = 1·0 mm: ——, present work; –·–, adiabatic collapse

pressure front gradually steepens, but the wave attenuates approximately in proportion to $1/r$ through the liquid. The peak pressure is lower than that in the adiabatic collapse and, at the position $r/R_0 = 1$, 58 atm (in the adiabatic case 63 atm). As a whole, present calculations support the earlier work (Hickling & Plesset 1964; Tomita & Shima 1977) both in the order of magnitude of the peak pressures and the pressure wave attenuation in inverse proportion to distance.

Figures 8(*a*) and (*b*) show the pressure distributions in liquid before and after the

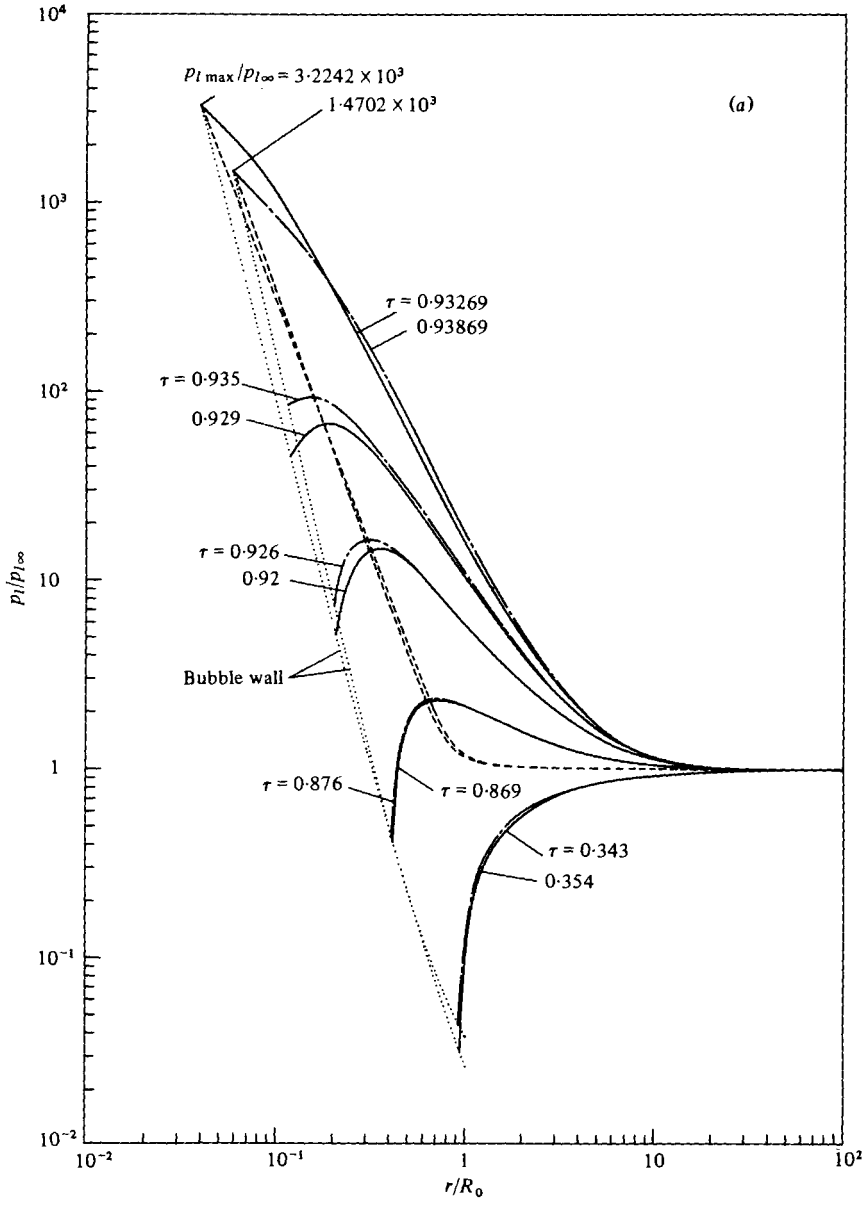

FIGURE 8 (*a*). For legend see facing page.

collapse of a bubble with initial radius $R_0 = 0{\cdot}1$ mm; initial conditions are the same as those in figures 2–7. The present bubble collapses to a much smaller radius in comparison with the adiabatic collapse, because the smaller bubbles show increased effects of heat conduction; the thermal diffusion length l within the bubbles will be proportional to $R_0^{\frac{1}{2}}$, and the ratio l/R_0 will vary as $R_0^{-\frac{1}{2}}$ (Hickling 1963). This results in a high collapse speed and a more violent collapse. The attained maximum impulsive pressure and gas temperature at the bubble centre are 2265 atm and 4151 K, respectively. The pressure is about twice that in the adiabatic collapse, whilst the temperature is about one-

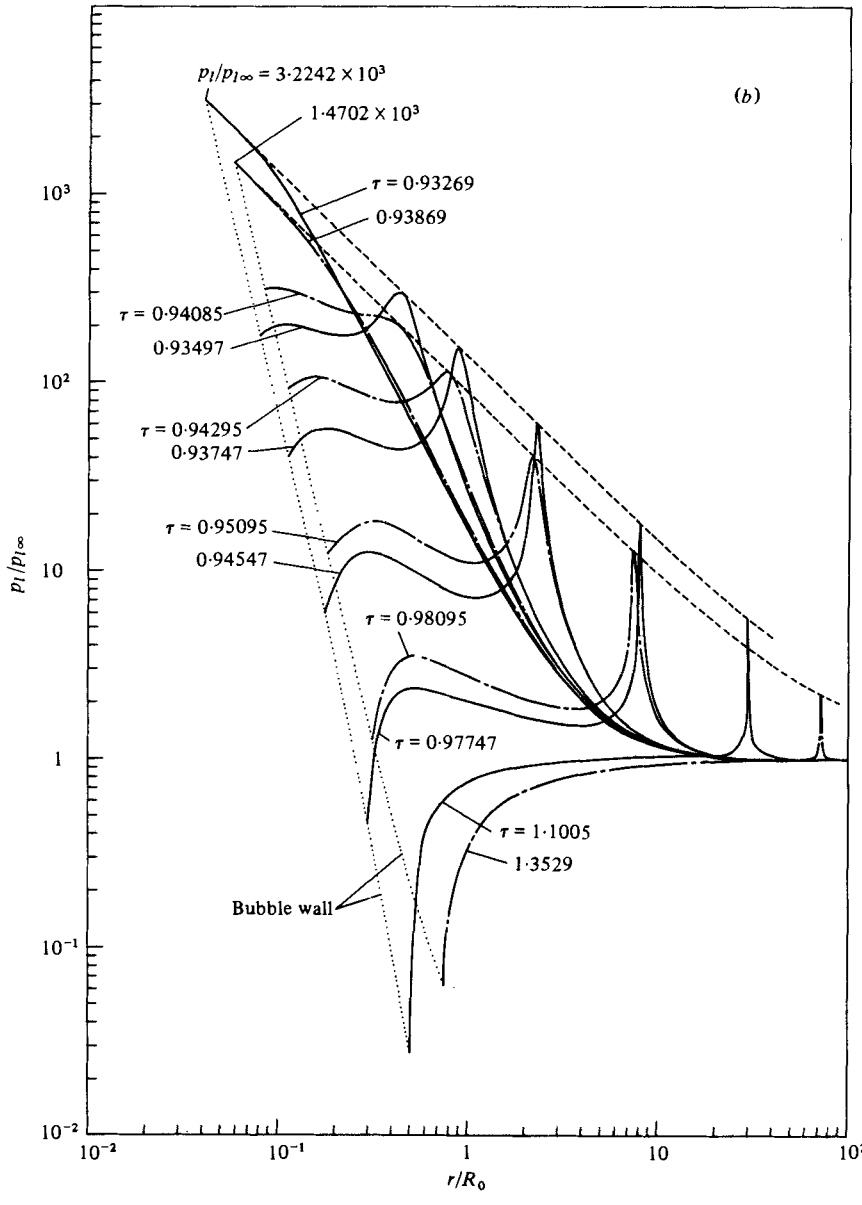

FIGURE 8. The pressure distributions in liquid (*a*) before and (*b*) after the collapse of a vapour–gas bubble with initial radius $R_0 = 0{\cdot}1$ mm: ——, present work; – · –, adiabatic collapse.

half of the temperature in that case. During rebound, a stronger pressure wave emanates into the liquid and its front steepens when compared with the adiabatic case. In fact, Efimov *et al.* (1976) experimentally demonstrated that bubbles smaller than 0·1 mm in diameter collapse in spherical form close to a solid boundary, and that the damage by these bubbles is caused by shock waves and accompanied with chemical corrosion.

Figures 9(*a*) and (*b*) similarly show the pressure distributions before and after the collapse of a bubble with initial radius $R_0 = 1{\cdot}0$ mm containing only the water vapour.

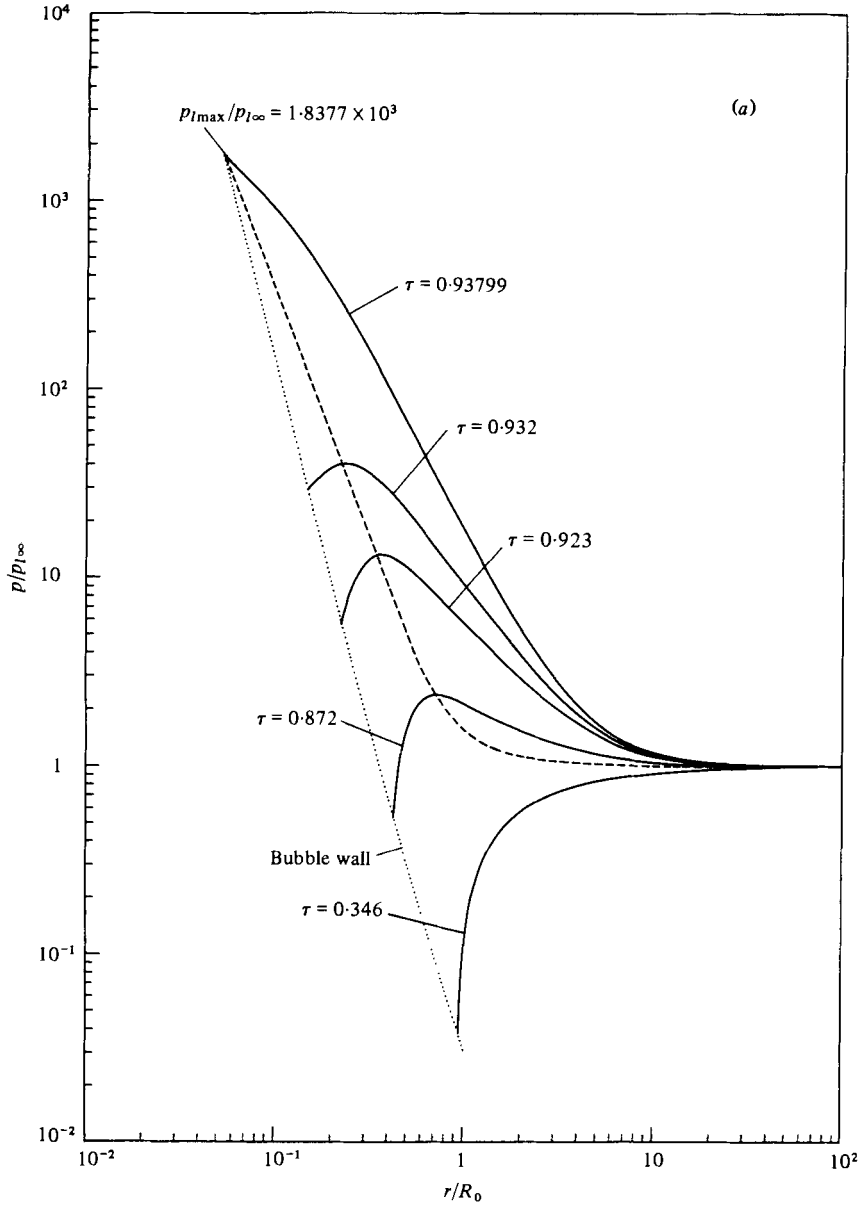

FIGURE 9(*a*). For legend see facing page.

The calculations are performed for the value $\alpha_M = 0{\cdot}01$. In this case, the maximum impulsive pressure $p_{li\max}$ is 1291 atm. The pressure at the instant when the bubble reaches its minimum radius is 12 atm at the position $r/R_0 = 1$. Meanwhile, the greatest pressure at the same position after the collapse is 67 atm. In case of the bubble collapsing near the solid boundary, the centre of the bubble approaches the boundary. So that the much stronger pressure wave is to be observed at the position of the boundary (Kling & Hammitt 1972; Lauterborn & Bolle 1975; Fujikawa & Akamatsu 1975,

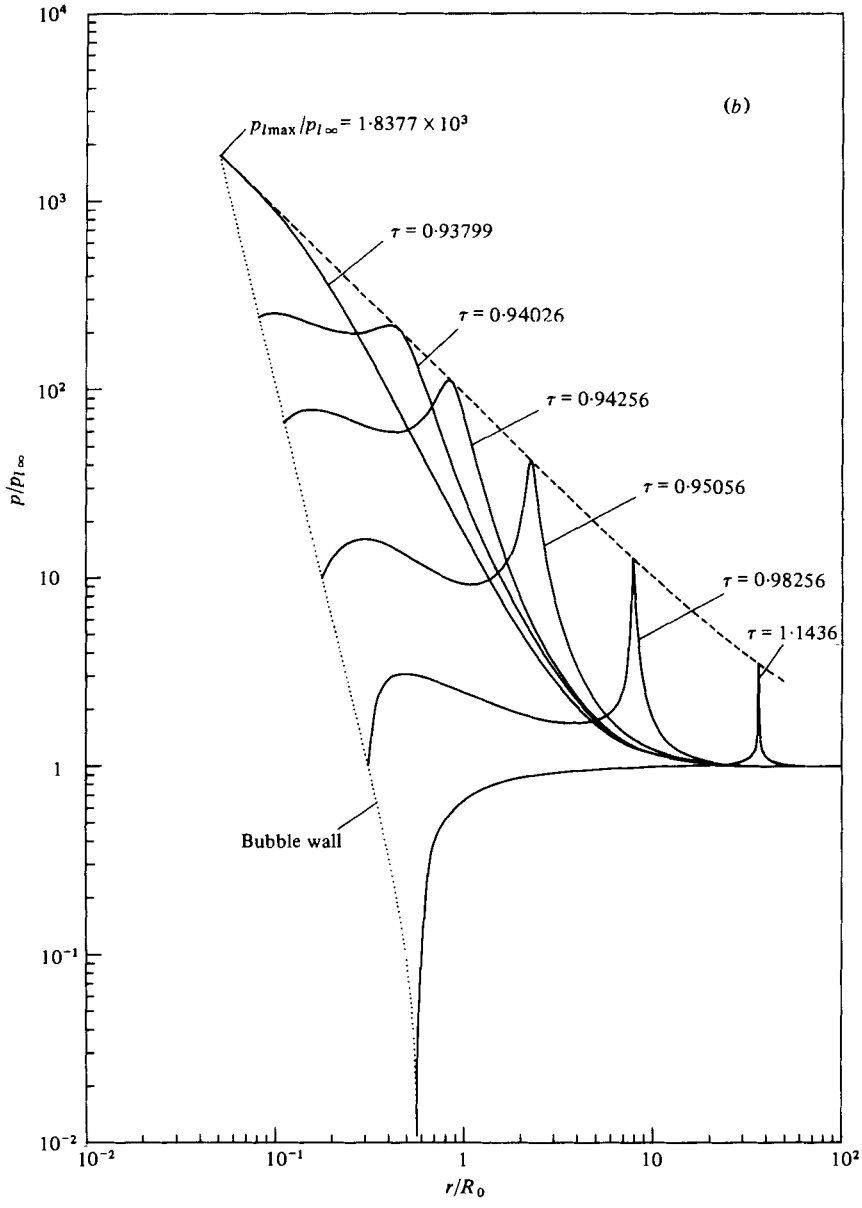

FIGURE 9. The pressure distributions in liquid (*a*) before and (*b*) after the collapse of a vapour bubble with initial radius $R_0 = 1{\cdot}0$ mm.

1978). Here, even a purely vaporous bubble proves to produce a pressure wave at the instant of the rebound. The mechanism can be explained as follows; at the initial stages of the collapse the vapour condenses back into the liquid, so that the vapour pressure in the bubble remains equal to a saturated vapour pressure. However, at the final stages the collapse takes place so rapidly that most of the vapour does not have enough time to condense. This remnant of vapour may then be compressed to a high

pressure, which will eventually become large enough to halt the inrushing liquid. Then the bubble rebounds and the pressure wave radiates into the liquid.

Table 2 shows the effects of the accommodation coefficient for evaporation and condensation on the attained minimum bubble-radius, the maximum pressures and temperatures within the bubble and at the interface, and the maximum rate of condensation through the interface. The suffixes min and max represent the minimum and maximum values respectively.

Table 2 (*a*) is concerned with a purely vaporous bubble. The values for $\alpha_M = 0{\cdot}04$ are shown in parentheses, because the assumption of thin thermal boundary layer may break down. The larger the value of α_M (i.e. the more rapidly the water vapour condenses), the smaller the radius to which the bubble collapses. As a whole, the attained minimum radius is small compared with the bubble containing the gas–vapour mixture. The smaller the radius to which the bubble collapses before the rebound, the greater the build-up of inertia in the liquid, and consequently the higher the inertial energy stored in the bubble as potential energy and then released to produce the stronger pressure wave into the liquid at the instant of rebound.

Table 2 (*b*) is concerned with a bubble containing both the water vapour and non-condensable gas. For $\alpha_M = 0{\cdot}1$ the bubble contracts to a much smaller radius compared with other values of α_M, while the interfacial temperature of the bubble contents $T_{mi\,\max}$ and the impulsive pressure $p_{li\max}$ reach the higher values. For $\alpha_M = 0{\cdot}04$ the liquid temperature $T_{li\max}$ and the rate of condensation $\dot{m}_{\max}$ at the interface are maxima respectively. According to the equation (7), in the case of $p_v \gg p_v^*$ (i.e. in the final collapse stages), the rate of condensation $\dot{m}$ is approximately proportional to the product of the coefficient α_M and the actual vapour pressure p_v. As shown in the table, this value is the largest for $\alpha_M = 0{\cdot}04$. The variation in liquid temperature is mainly produced by release of the latent condensation heat. The temperature of the bubble contents at the centre becomes higher as the coefficient α_M increases. A bubble containing the water vapour and gas seems to collapse not so straightforward as a bubble containing only the water vapour.

4. Experiments

Extensive experiments on collapsing behaviour of single, twin and triadic bubbles near the solid boundary were previously performed in a water shock tube (Fujikawa & Akamatsu 1975, 1978). Principal results observed by pressure gauges and high-speed photographs can be summarized as follows: (1) the water jet does not produce any detectable effects; (2) the impulsive pressure is brought about by the shock wave; (3) the shock intensity is of the order of 10^4 atm, and its duration $2 \sim 3$ μs. Here, the authors will further offer supplemental evidences for these conclusions by means of dynamic photoelasticity.

4.1. *Apparatus*

The authors have already given a detailed description of their water shock tube (Fujikawa & Akamatsu 1975, 1978). So they will explain only the present experimental method. In the water-filled shock tube, bubbles expand to maximum radii under the action of expansion waves, and then collapse under successive compression waves. The collapse and rebound of bubbles situated at various distances from the solid boundary of a photoelastic material are observed by means of photoelastic technique.

(*a*) Bubble containing water vapour only (initially saturated)

α_M	$10^2 R_{min}$ (mm)	$\frac{p_{v max}}{p_{l\infty}}$	$\frac{p_{li max}}{p_{l\infty}}$	$\frac{T_{li max}}{T_{l\infty}}$	$\frac{T_{mi max}}{T_{l\infty}}$	$\frac{T_{mc max}}{T_{l\infty}}$	$10^3 \dot{m}_{max}$ (g mm^{-2} s^{-1})
0·04	(2·102)	(11938)	(11940)	(2.208)	(78·26)	(106·1)	(−3628)
0·01	4·988	1838	1838	1·961	10·27	12·87	−380·9
0	6·842	869·6	869·6	1·056	6·668	8·495	0

(*b*) Bubble containing water vapour (initially saturated) and air

α_M	$10^2 R_{min}$	$\frac{p_{v max}}{p_{l\infty}}$	$\frac{p_{g max}}{p_{l\infty}}$	$\frac{p_{li max}}{p_{l\infty}}$	$\frac{T_{li max}}{T_{l\infty}}$	$\frac{T_{mi max}}{T_{l\infty}}$	$\frac{T_{mc max}}{T_{l\infty}}$	$10^3 \dot{m}_{max}$ (g mm^{-2} s^{-1})
1·0	5·686	0·8162	1577	1578	1·125	12·73	29·02	−1·181
0·1	5·599	5·371	1612	1617	1·174	13·50	28·33	−10·22
0·04	5·738	203·8	1207	1411	1·617	11·64	22·86	−141·6
0·01	7·443	422·6	250·4	673·0	1·538	6·701	10·33	−118·8
0	9·089	316·5	96·47	412·9	1·058	5·233	7·851	0
Adia. & equi.	5·880	0·03281	1470	1470	1·000	29·97	29·97	0

TABLE 2. The effects of accommodation coefficient for evaporation or condensation on the attained minimum bubble radius, the maximum pressures and temperatures both inside and outside the bubble, and the maximum rate of condensation through the phase interface. (*a*) The bubble contains only water vapour (initially saturated) ($R_0 = 1{\cdot}0$ mm, $p_{v0} = 23{\cdot}05 \times 10^{-3}$ atm, $p_{l\infty} = 0{\cdot}7025$ atm, $T_{l\infty} = 293{\cdot}15$ K). (*b*) The bubble contains water vapour (initially saturated) and air ($R_0 = 1{\cdot}0$ mm, $p_{v0} = 23{\cdot}05 \times 10^{-3}$ atm, $p_{g0} = 7{\cdot}025 \times 10^{-3}$ atm, $p_{l\infty} = 0{\cdot}7025$ atm, $T_{l\infty} = 293{\cdot}15$ K).

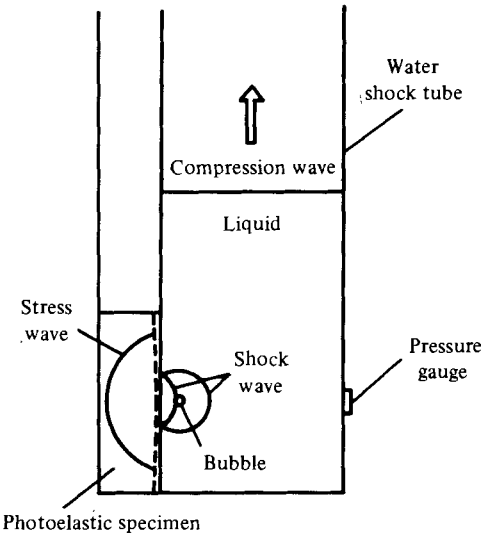

FIGURE 10. The configuration of the photoelastic specimen relative to the bubble and the pressure gauge.

Figure 10 shows the configuration of a photoelastic specimen relative to a bubble and a pressure gauge. The specimen is fabricated with 12×8 mm, 6 mm-thick epoxy resin (photoelastic sensitivity: 1·00 mm kg^{-1}) of stress wave velocity 2600 m s^{-1}. The pressure gauge with high response is flush mounted with the tube wall opposite to the photoelastic specimen and is used to detect the instant of arrival of the shock wave radiated from the bubble. The distance from the surface of specimen to the pressure gauge is just 15·6 mm. Given the speed of sound in water as 1483 m s^{-1} (at 20 °C), it takes 10·57 μs for the shock wave emanating from the bubble to reach the pressure gauge; that is, the shock wave is to have been radiated from the bubble, 10·57 μs before the impulsive pressure is detected by the present pressure gauge. The pulsed organic dye laser is employed as a light source with the pulse width of 0·3 μs. The pressure history in the test section and the instant of laser emission are recorded on the same time base of the synchronoscope.

4.2. *Experimental results and discussions*

4.2.1. *Microjet formation and shock wave radiation.* Figure 11 (plate 1) shows typical high-speed photographs of a spherical bubble collapsing close to a solid boundary. The bubble is produced at a distance $L = 1{\cdot}80$ mm from the boundary and reaches a maximum radius $R_0 = 0{\cdot}95$ mm; the ratio $L/R_0 = 1{\cdot}89$. Frames are consecutive, and follow one another from left to right. The time elapsed from the start of collapse is marked under each of the frames. During collapse, the bubble loses spherical symmetry by flattening on the bubble wall opposite to the solid boundary. As a result of a higher collapse speed of the upper bubble wall, a microjet can be expected to be produced, penetrating the bubble towards the boundary; the jet, inside the bubble, is invisible because these frames are shadow pictures taken by a Cranz–Shardin camera. The funnel-shaped protrusion, visible as a fine dark line, is a secondary effect produced by the jet impingement on the lower bubble wall. This is called 'tip' and distinguished

from 'true jet' (Lauterborn & Bolle 1975). Whether the true jet and the tip can produce impulsive pressures will be clarified in § 4.2.2.

Figures 12 (*a*) and (*b*) (plate 1) show representative pictures of shock waves radiated from bubbles (*a*) close to, or (*b*) in contact with, the solid boundary. These results clearly demonstrate that the presence of a solid boundary does not inhibit the rebound of a vaporous bubble and the resulting shock wave radiation.

4.2.2. *Stress fringes, in the photoelastic material, caused by the bubble collapse.* Figures 13 (*a*) and (*b*) (plate 2) show typical high-speed photographs of bubbles in contact with, or close to, the solid boundary. The impulsive pressure due to the bubble collapse and the signal of laser emission are recorded on each oscillogram. The picture marked with the underlined time index was taken by just the timed laser-emission.

The isochromatic fringe patterns in the specimen due to the stress wave, as shown in figure 13 (*a*), are originated by the second rebound of the bubble initially in contact with the solid boundary. The signal of the impulsive pressure due to the first rebound of the bubble triggers, through a variable delay unit, a laser flash lamp so that the stress waves due to the second rebound of the bubble are photographed at any stage of their propagation. In particular, the fifth frame shows that the stress-wave propagates 3·5 mm after its appearance on the specimen. The wave velocity being 2600 m s^{-1} in epoxy resin, the present stress wave had been generated on the surface of the photoelastic specimen, 1·34 μs before this photograph was taken. On the contrary, the corresponding oscillogram shows that the laser light was emitted at the instant that 1·31 μs elapsed after the shock wave (second impulsive pressure) radiated from the bubble; the time difference between the laser signal and the second impulsive pressure is 9·26 μs and it takes 10·57 μs for the shock wave to reach the pressure gauge (figure 10) situated on the opposite wall. The difference in time 0·03 μs is within the limit of experimental error. Therefore, the present stress wave in the specimen proves to be caused by the shock wave emanated at the instant of the bubble rebound. It must be noted here that no isochromatic fringe patterns are recognized in the specimen before the bubble rebounds (second and third frames) although the bubble collapses in such a situation that the jet is expected to directly impinge on the boundary. Therefore, the strength of the jet may be inferred to be much less than the shock intensity. The sensitivity, with respect to the spatial extension, of the specimen may be sufficient to detect the impact of the jet, judging from the fact that the stress wave caused by a shock wave emanated at the minute bubble size ($< 0{\cdot}1$ mm in radius (Fujikawa & Akamatsu (1978)) can be clearly observed.

The behaviour of a bubble in the vicinity of the boundary is shown in the figure 13 (*b*). The bubble is produced at a distance $L = 3{\cdot}20$ mm from the boundary and reaches a maximum radius $R_0 = 2{\cdot}76$ mm; the ratio $L/R_0 = 1{\cdot}16$. Even in the present situation, very close to the solid boundary the jet, on the upper bubble wall, does not directly strike the boundary. During rebound, the bubble approaches the boundary forming the tip and finally attaches to the solid surface. The second frame clearly indicates that the stress fringes are caused in the photoelastic specimen before the tip reaches the surface. These fringes originate from the impact of shock wave radiated at the instant of bubble rebound, as the authors pointed out in their previous papers (Fujikawa & Akamatsu 1975, 1978). The shock intensity on the boundary is of the order of 10^2 atm, from the results in the preceding chapter, provided that the bubble collapses in spherical form.

From the above observations, we conclude that the impulsive pressure is caused by the shock wave radiated into the liquid at the instant of the rebound of the collapsing bubble, and that the jet impingement does not produce any perceivable effects.

5. Conclusions

First, a set of equations has been obtained to predict the dynamical behaviour of a cavitation bubble in a liquid. The present formulation takes into account the effects of compressibility of the liquid, nonequilibrium condensation of the vapour, heat conduction and temperature discontinuity at the phase interface.

Secondly, numerical analyses have been made of the effect of non-equilibrium condensation of water vapour in a vapour–gas bubble collapsing in water. It has been found that the temperature gradient develops inside the bubble owing to heat conduction through the interface, and that the combinations of the condensing water vapour and non-condensable gas have a very strong influence on the behaviour of collapsing bubble and the radiated pressure wave. The calculations indicate further that a purely vaporous bubble may produce a strong pressure wave in the liquid at the instant of the rebound.

Thirdly, the stress wave, both in a solid and a liquid, due to the collapse of a single bubble has been observed in detail by means of the dynamic photoelastic technique. The present experimental evidences also support our previous observations that the impulsive pressure accompanying the bubble collapse is caused by the shock wave radiated into the liquid from the bubble, and that the jet impingement does not produce any detectable effects.

Continuation of the present numerical calculations will reveal the effects of the initial bubble radius, liquid temperature, and applied ambient pressure in the liquid on the collapse of the cavitation bubble.

This research was carried out partly with the Grants in Aid for Scientific Research of the Ministry of Education in Japan both in 1976 and 1978. The authors wish to express their gratitude for these grants.

Appendix. The thickness of the thermal boundary layer outside the bubble wall

The principal difficulty in the analysis of heavy bubble collapse is that, unlike the case of growth, the thickness of the liquid layer cannot in general be taken to be small compared with the bubble radius for all times (Plesset & Prosperetti 1977).

Let us here estimate approximately the thickness of the liquid layer surrounding the bubble wall and also consider an applicable limitation of thermal boundary-layer approximation adopted in the present paper. For analytical simplicity, assuming that the temperature profile in the liquid layer is a parabolic curve and that the heat conduction inside the bubble is negligible, then the thickness of the liquid layer δ_l can be expressed as follows (Mitchell 1970; Mitchell & Hammitt 1974):

$$\frac{\delta_l}{R} \approx \frac{D_l L(\rho_v(R) R^3 - \rho_v(R_0) R_0^3)}{\lambda_l (T_{l\infty} - T_{li}) R^3}, \tag{A 1}$$

where the notation is the same as used in the body of this paper. Estimating the equation (A 1) for a purely vaporous bubble in the final stage of collapse, for example with $R_0 = 1$ mm, $R \approx 0{\cdot}05$ mm, $\rho_v(R_0) \approx 1{\cdot}7 \times 10^{-5}$ g cm^{-3}, $\rho_v(R) \approx 9{\cdot}1 \times 10^{-2}$ g cm^{-3}, $T_{l\infty} = 293$ K, and $T_{li} \approx 575$ K (for $\alpha_M = 0{\cdot}01$ in table 2(*a*)), we obtain

$$\delta_l/R \approx 9{\cdot}0 \times 10^{-2} < 1.$$

However, for larger values of α_M, this inequality (that is, the assumption (7)) may break down because bubbles contract to smaller radii. For $\alpha_M = 0{\cdot}04$ in table 2(*a*), the numerical results (in parentheses) are listed for comparison with those for other values of α_M. Concerning vapour and gas bubbles as shown in table 2(*b*), the liquid layer thickness is of the order of a few-tenths of the minimum bubble radius. The zero-order solution of Plesset & Zwick (1952) may be inadequate to obtain the bubble surface temperature. In the present analysis, a first-order correction is made for the zero-order solution. Neverthless, in the final stage of the collapse, the bubble wall temperature may be estimated larger by a few per cent than an exact solution because the latent heat of condensation, in the thermal boundary-layer approximation, is taken to be stored only in the thin liquid layer.

REFERENCES

Alty, T. 1936 *Sci. Prog. Lond.* **31**, 436.

Alty, T. & Mackay, C. A. 1935 *Proc. Roy. Soc.* A **149**, 104.

Benjamin, T. B. 1958 *Proc. 2nd Symp. on Naval Hydrodyn., Washington*, p. 207.

Benjamin, T. B. & Ellis, A. T. 1966 *Phil. Trans. R. Soc.* A **260**, 221.

Cole, R. H. 1948 *Underwater Explosions*. New York: Dover.

Ebeling, K. J. & Lauterborn, W. 1977 Paper presented at *Euromech* 98, Eindhoven.

Efimov, A. V., 1976 *Proc. IAHR Symp. Grenoble*, p. 159.

Ellis, A. T. 1956 *Proc. Symp. Cavitation in Hydrodyn., N.P.L.*, paper 8. London: H.M.S.O.

Flynn, H. G. 1975*a* *J. Acoust. Soc. Am.* **57**, 1379.

Flynn, H. G. 1975*b* *J. Acoust. Soc. Am.* **58**, 1160.

Fujikawa, S. & Akamatsu, T. 1975 *Proc. 10th Int. Shock Tube Symp., Kyoto*, p. 174.

Fujikawa, S. & Akamatsu, T. 1978 *Bull. Japan Soc. Mech. Eng.* **21**, 223.

Hatsopoulos, G. N. & Keenan, J. H. 1965 *Principles of General Thermodynamics*. Wiley.

Herring, C. 1941 *Office of Sci. Res. & Develop. Rep.* no. 236.

Hickling, R. 1963 *J. Acoust. Soc. Am.* **35**, 7.

Hickling, R. & Plesset, M. S. 1964 *Phys. Fluids* **7**, 7.

Hill, P. G. 1966 *J. Fluid Mech.* **25**, 593.

Hsieh, D. Y. 1965 *Trans. A.S.M.E.* D, *J. Basic Engng* **87**, 991.

Jahsman, W. E. 1968 *Trans. A.S.M.E.* E, *J. Appl. Mech.* **35**, 579.

Jones, I. R. & Edwards, D. H. 1960 *J. Fluid Mech.* **7**, 596.

Kennard, E. H. 1938 *Kinetic Theory of Gases*. McGraw-Hill.

Kling, C. L. & Hammitt, F. G. 1972 *Trans. A.S.M.E.* D, *J. Basic Engng* **94**, 825.

Knacke, A. & Stranski, I. N. 1956 *Prog. Metal Phys.* **6**, 181.

Kogan, M. N. 1969 *Rarefied Gas Dynamics*. Plenum.

Kornfeld, M. & Suvorov, L. 1944 *J. Appl. Phys.* **15**, 495.

Kuttruff, H. 1962 *Acustica* **6**, 526.

Lauterborn, W. & Bolle, H. 1975 *J. Fluid Mech.* **72**, 391.

Mitchell, T. M. 1970 Ph.D. Thesis, Depart. of Nuclear Engng, Univ. of Michigan.

Mitchell, T. & Hammitt, F. G. 1974 *Nucl. Sci. Engng* **53**, 263.

MORI, Y. 1973 *Trans. Japan Soc. Mech. Eng.* **39**, 694.

NAUDÉ, C. F. & ELLIS, A. T. 1961 *Trans. A.S.M.E.* D, *J. Basic Engng* **83**, 648.

PLESSET, M. S. 1949 *J. Appl. Mech.* **16**, 277.

PLESSET, M. S. & CHAPMAN, R. B. 1971 *J. Fluid Mech.* **47**, 283.

PLESSET, M. S. & PROSPERETTI, A. 1976 *J. Fluid Mech.* **78**, 433.

PLESSET, M. S. & PROSPERETTI, A. 1977 *Ann. Rev. Fluid Mech.* **9**, 145.

PLESSET, M. S. & ZWICK, S. A. 1952 *J. Appl. Phys.* **23**, 95.

RAYLEIGH, LORD 1917 *Phil. Mag.* **34**, 94.

SCHRAGE, R. W. 1953 *A Theoretical Study of Interphase Mass Transfer*. Columbia University Press.

SHIMA, A. & NAKAJIMA, K. 1977 *J. Fluid Mech.* **80**, 369.

THEOFANUS, T. G. 1969 Paper presented at *11th Nat. Heat Transfer Conf., Mineapolis.*

TOMITA, Y. & SHIMA, A. 1977 *Bull. Japan Soc. Mech. Eng.* **20**, 1453.

TRILLING, L. 1952 *J. Appl. Phys.* **23**, 14.

ZWICK, S. A. & PLESSET, M. S. 1955 *J. Math. Phys.* **33**, 308.

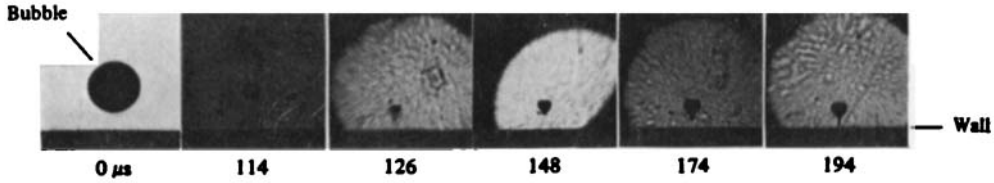

FIGURE 11. Microjet formation from the bubble in the neighbourhood of the solid boundary.

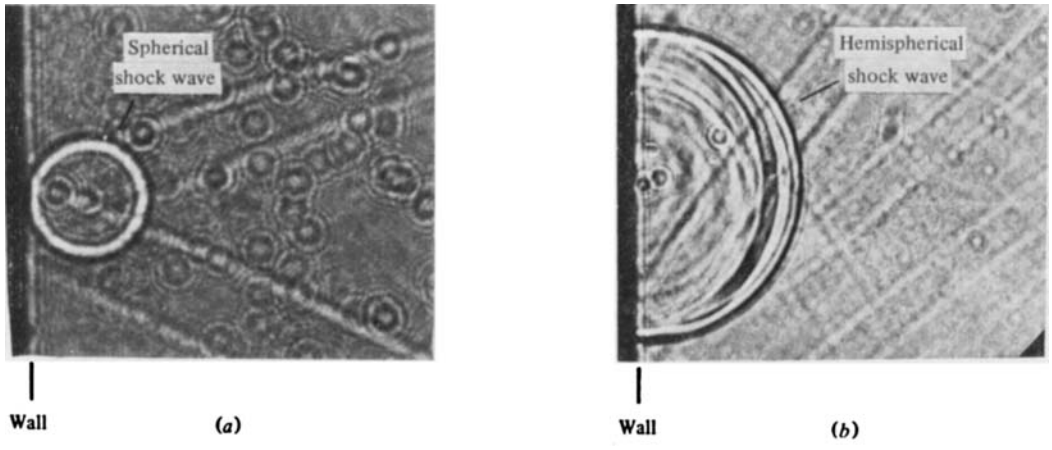

FIGURE 12. The photographs of the shock waves emanating from the bubbles (*a*) close to, or (*b*) in contact with, the solid boundary.

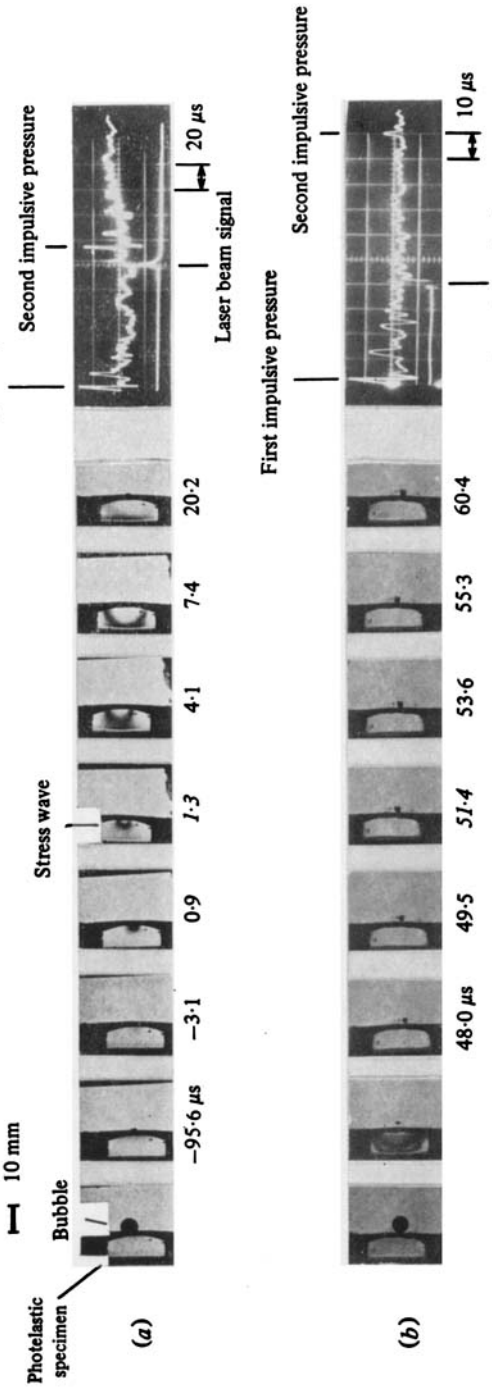

FIGURE 13. The isochromatic fringe patterns in photoelastic specimen due to the stress waves originated by the bubbles collapsing, (*a*) in contact with, and (*b*) in the neighbourhood of the specimen surface.